Review

Review of Bathymetric Surveying and Mapping Techniques

Ninfa Arianna Speciale , Mauro Lo Brutto , Giuseppe Ciraolo , Antonino Maltese *

Posted Date: 4 June 2026

doi: 10.20944/preprints202606.0385.v1

Keywords: bathymetry; multibeam echo sounder; single-beam echo sounder; acoustic remote sensing; airborne LiDAR bathymetry; satellite-derived bathymetry; radar altimetry; radar altimetry; wave-spectrum bathymetry

 doi:10.20944/preprints202606.0385.v1

Review

Review of Bathymetric Surveying and Mapping Techniques

Ninfa Arianna Speciale, Mauro Lo Brutto, Giuseppe Ciraolo and Antonino Maltese *

Department of Engineering (DI), Università degli Studi di Palermo, 90128 Palermo, Italy

* Correspondence: antonino.maltese@unipa.it

Highlights

What are the main findings?

- A comprehensive comparison of acoustic, optical, LiDAR, radar-altimetric, wave-spectrum and other techniques reveals that no single method is universally optimal across all marine environments.
- The review identifies the key factors controlling spatial resolution, vertical accuracy, and data reliability, highlighting how acquisition and processing choices directly influence bathymetric quality.

What are the implications of the main findings?

- Integrated multi-sensor approaches, combining acoustic, optical, LiDAR, and altimetric data, could represent the most effective strategy to enhance completeness and accuracy in seafloor mapping.
- Improved acquisition technologies and autonomous platforms are expected to accelerate global bathymetric coverage, supporting initiatives such as Seabed 2030 and advancing marine geomatics applications.

Abstract

Bathymetric information is essential for navigation safety, coastal engineering, marine habitat mapping, seafloor characterization, and climate-related studies. However, despite major international efforts, to date, only 27.3% of the world's ocean floor has been mapped in accordance with modern hydrographic standards, underscoring the need for more comprehensive and higher-resolution seafloor data. This review provides an integrated assessment of the main techniques used for bathymetric data acquisition, examining their physical principles, operational constraints, data-processing workflows, and accuracy drivers. The analysis covers acoustic methods, including single-beam, multibeam, and interferometric sonars, optical approaches based on electromagnetic radiation, airborne LiDAR bathymetry, radar altimetry, and wave-spectrum-based techniques, together with a set of unconventional and emerging methods that offer additional flexibility in challenging or data-poor environments. For each category, the review discusses achievable spatial and vertical resolution, environmental limitations, platform-dependent constraints, and the influence of water properties on measurement reliability. Attention is given to data-processing steps such as sound-speed correction, motion compensation, filtering, and interpolation, which strongly affect the quality of the final bathymetric product. A comparative synthesis highlights that no single technique is generally optimal: acoustic systems remain the most accurate and versatile, while optical and LiDAR methods excel in shallow, clear waters. The analysis indicates that synergistic use of complementary techniques, leveraging the strengths of each sensing principle, is essential to produce bathymetric datasets tailored to the specific requirements of diverse mapping applications.

Keywords: bathymetry; multibeam echo sounder; single-beam echo sounder; acoustic remote sensing; airborne LiDAR bathymetry; satellite-derived bathymetry; radar altimetry; radar altimetry; wave-spectrum bathymetry

 doi:10.20944/preprints202606.0385.v1

1. Introduction

design, monitoring, and management of coastal engineering infrastructures [1,2]; characterizing and mapping the spatial distribution of benthic habitats [3]; documenting and safeguarding submerged archaeological sites [1]; providing essential information for defense and military operations [4]; and contributing to assessments of climate-change impacts on coastal and marine systems [5].

Depending on the intended application, bathymetric datasets must meet specific technical requirements for temporal, spatial, and vertical accuracy to ensure consistency, reliability, and suitability for downstream analyses. In this context, Hell et al. 2012 [6], based on a survey conducted among public agencies, academic institutions, and research organizations, propose a classification of the spatial resolutions most appropriate for different bathymetric applications, as illustrated in Table 1.

Table 1. Spatial resolution requirements for different application domains. Adapted from Hell et al. (2012) [6].

Application	Spatial resolution [m]	Vertical accuracy	Notes
Marine archaeology / Geotechnics	Decimetres - 1	0.1 m (shallow water), 0.25 m (elsewhere)	Requires very high point density; high vertical accuracy required.
Habitat Mapping / Natural Resources	2 - 50		For habitats and species, a resolution of >25 m is considered insufficient.
Coastal planning / Infrastructure			/
Hydrodynamic modelling / Ocean circulation	100 or coarser*		Requires continuous and extensive coverage. Coarse resolutions acceptable for large-scale studies.

* In the case of coastal hydrodynamic circulation modelling, higher bathymetric resolutions are nevertheless required, typically on the order of 10 m [7].

Given the relevance of the topic, two key questions naturally arise:

- Do the bathymetric datasets currently available meet the requirements of the wide range of existing applications?
- Which acquisition and data-processing techniques can produce bathymetric information that is suitable for the intended application?

The study was conducted as a scoping review, following the methodological framework of the PRISMA Extension for Scoping Reviews (PRISMA-ScR) [8]. The adopted methodology, including the PRISMA 2020 flow diagram (Adapted from: Gizachew et al. (2026) [9]), search strategy, inclusion criteria, considerations on methodological strategy, and the PRISMA 2020 Checklist, are described in the Supplementary Materials section.

This review aims to provide a synthesis of the principal bathymetric acquisition methods, describing their data-collection and processing workflows, and examining the factors that influence spatial and vertical resolution, as well as measurement accuracy. The ultimate objective is to establish objective criteria to support the selection of the most appropriate technique in relation to the environmental characteristics of the study area and the required data-quality standards. Attention is given to acquisition modalities and processing strategies, as these elements play a decisive role in error propagation and, consequently, in the quality of the final bathymetric product.

 doi:10.20944/preprints202606.0385.v1

A central reading key to this review is the depth-dependent applicability of each bathymetric technique. For this reason, the manuscript systematically recalls the underlying physical principles and governing equations of each method, clarifying the depth ranges in which they can provide accurate and reliable measurements.

For ease of consultation, the review is organized into thematic sections. Section 2 provides an overview of the main actors, data sources, and operational levels involved in bathymetric data acquisition, establishing the contextual framework for the subsequent analysis of individual techniques. Section 3 examines acoustic techniques, which represent the core of high-accuracy seafloor mapping. Section 4 discusses optical bathymetry, including passive optical methods, photogrammetric approaches, and airborne LiDAR bathymetry. Section 5 presents wave-spectrum-based bathymetry, while Section 6 addresses radar-altimetric approaches for large-scale observations. Section 7 introduces emerging and unconventional techniques.

Sections 2 to 6 are organized according to an overall progression from techniques that provide higher spatial resolution and operate in shallower waters toward methods applicable over increasingly large depth ranges and usually providing lower spatial resolution. This reading key is not to be interpreted strictly, as each section may include multiple techniques with different performance characteristics.

Within each methodological section, the principles of data processing are first described, followed by an examination of the factors influencing measurement reliability.

Section 8 provides a comparative assessment of all methods, and Section 9 illustrates representative applications. Finally, Section 10 summarizes the main insights and offers guidance for selecting the most appropriate technique according to environmental conditions and accuracy requirements.

2. Bathymetric Data Acquisition

This section outlines the organizational and operational framework supporting modern bathymetric data acquisition. It reviews the main actors, data repositories, and initiatives involved, and describes how efforts ranging from global programs to local surveys influence the availability, resolution, and accessibility of bathymetric data.

Indeed, bathymetric data acquisition is a multi-layered process involving a wide range of actors and operational levels (Figure 1), each with clearly defined roles and responsibilities [4]. A clear understanding of this system is essential for selecting appropriate data sources and identifying the most suitable information for the intended application.

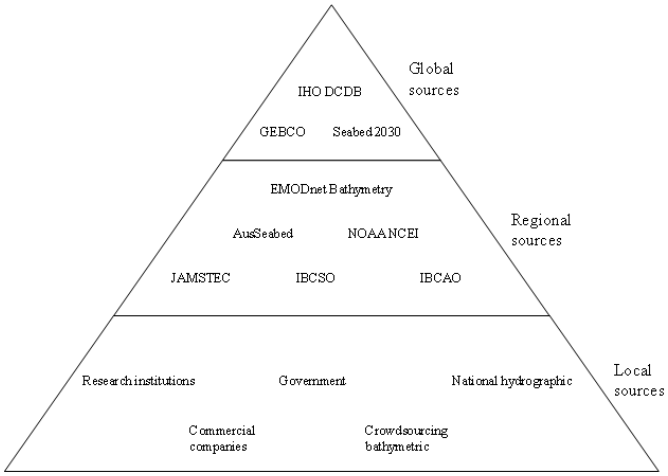

Figure 1. Actors and Operational Levels in Bathymetric Data Acquisition.

Among the key global actors, the International Hydrographic Organization (IHO) [10] plays a central role in coordinating worldwide hydrographic activities. Its primary mission is to ensure

 doi:10.20944/preprints202606.0385.v1

navigation safety by promoting the standardization and harmonization of hydrographic information and nautical charting. Beyond its technical and cartographic mandate, the organization also defines the regulatory and infrastructural framework for data collection and dissemination through the Data Centre for Digital Bathymetry (DCDB) [11], a global digital repository containing more than 70 terabytes of bathymetric data.

Another major international reference is the General Bathymetric Chart of the Oceans (GEBCO) [12] program, whose main objective is to provide a coherent and up-to-date global representation of the seafloor through the production of standardized Bathymetric Digital Elevation Models. GEBCO's most recent product is the Type Identifier Grid GEBCO_2024, which specifies the data source for each grid cell at a geometric resolution of 15 arc-seconds (~500 m) [13]. GEBCO has also developed an experimental multi-resolution grid (up to 100 m), integrating higher-resolution bathymetric datasets where available. At present, this version is limited to selected pilot areas, including offshore regions of Australia, waters surrounding New Zealand, and the Hawaiian archipelago [14].

Supporting GEBCO's activities is the Seabed 2030 initiative [15], which aims to facilitate the complete mapping of the global ocean floor by 2030 through the acquisition of new bathymetric data and the integration of existing datasets. After processing and quality control, the collected data are contributed to the DCDB and incorporated into GEBCO's global grids.

In addition to global organizations, a wide network of regional initiatives provides higher-resolution bathymetric datasets for specific geographic areas. A selection of these initiatives is reported below, detailing each the geographic coverage, spatial resolution, and corresponding access portal (Table 2).

Table 2. Regional initiatives, geographic coverage, spatial resolution, and portal access links.

Name	Geographic area	Spatial resolution (m)	Link
European Marine Observation and Data Network Bathymetry (EMODnet Bathymetry)	Europe, North-East Atlantic, Mediterranean, Baltic Sea, Black Sea	~ 100	[16]
AusSeabed	Australia	For the AusBathyTopo series: 30, 100 or 250	[17]
Japan Agency for Marine-Earth Science and Technology (JAMSTEC)	South and Western Pacific Ocean	Several (contribution to Seabed 2030)	[18]
NOAA National Centers for Environmental Information (NCEI)	United States	From a few metres to hundreds, variables that can be consulted through the portal	[19]
International Bathymetric Chart of the Southern Ocean (IBCSO)	Antarctica	500	[20]
International Bathymetric Chart of the Arctic Ocean (IBCAO)	Arctic Region	200	[21]

Finally, the last operational level consists of local initiatives, which focus on geographically restricted areas, such as bays, harbors, coastal stretches, or environmentally sensitive marine zones, and produce very high-resolution bathymetric data. These initiatives are promoted by a diverse range of actors, including: i) research institutions; ii) government agencies; iii) national hydrographic offices, sometimes embedded within military structures, which operate primarily within Exclusive Economic Zones, and, in these cases, data access may be restricted for security reasons; iv) commercial surveying companies contracted by public or private entities; v) crowdsourced bathymetry, an approach promoted by the IHO that involves conventional vessels equipped with echo sounders and operated by professional crews.

 doi:10.20944/preprints202606.0385.v1

In Europe, the three main communities responsible for providing bathymetric data are national hydrographic offices, research institutions, and private industry [22]. A selection of these initiatives is illustrated in Table 3, together with their geographic coverage, spatial resolution, and corresponding access portals.

Table 3. Local Some local initiatives, geographic coverage, spatial resolution, and portal access links.

Name	Geographic area	Spatial resolution [m] up to:	Link
Mareano	Norway	5	[23]
Istituto Idrografico della Marina (IIM)	Italy	10	[24]
Bundesamt für Seeschifffahrt und Hydrographie (BSH)	Germany	50	[25]

Despite extensive national and international efforts dedicated to acquiring new surveys, processing data, and continuously creating, archiving, and updating seafloor maps, only 27.3% of the global ocean floor has been mapped according to modern standards [15]. Considering that the global ocean covers 71% of the Earth's surface, approximately 362 million km² [26] the area currently mapped amounts to roughly 98.8 million km².

Moreover, high-resolution bathymetric sources, produced primarily by actors operating at the local level, are often difficult to access due to security restrictions, economic considerations, or national regulatory constraints [4]. In line with these limitations, Hell et al., 2012 [6] report that most users highlight low resolution and insufficient bathymetric coverage, particularly in shallow waters, along with data-access issues (especially in Sweden) and concerns related to accuracy, metadata completeness, and harmonization across datasets.

Finally, bathymetry varies over time with periodicities ranging from daily to centennial scales, driven by site-specific hydrodynamic processes (e.g., erosion and sediment deposition) [27], geological mechanisms (e.g., post-rift thermal subsidence and dynamic uplift) [28], biological activity (e.g., formation of biogenic structures) [29], and/or anthropogenic interventions (e.g., dredging, land reclamation) [30]. This makes it necessary to analyze bathymetric datasets acquired at different times to assess temporal changes and derive a Digital Elevation Model of Difference [31].

2.1. Bathymetric Surveys Techniques

Bathymetric surveys may be conducted using a variety of techniques, each characterized by differing capabilities in investigating water bodies with specific physical properties (e.g., depth, water clarity, and transmissivities), as well as by the spatial and temporal resolution they can achieve and the technological and operational resources they require. As a result, the selection of the most appropriate technique is inherently dependent on the characteristics of the operational environment and the specific objectives of the survey. Coastal and shallow-water settings (<50 m), for instance, constitute particularly complex environments influenced by wave energy, coastal hydrodynamics, and rapidly varying seabed morphology. These conditions typically demand high-resolution methods capable of delivering enhanced altimetric and planimetric detail to meet application-driven requirements [6].

The evolution of measurement sensors used in bathymetric surveying over time is shown in Figure 2.

 doi:10.20944/preprints202606.0385.v1

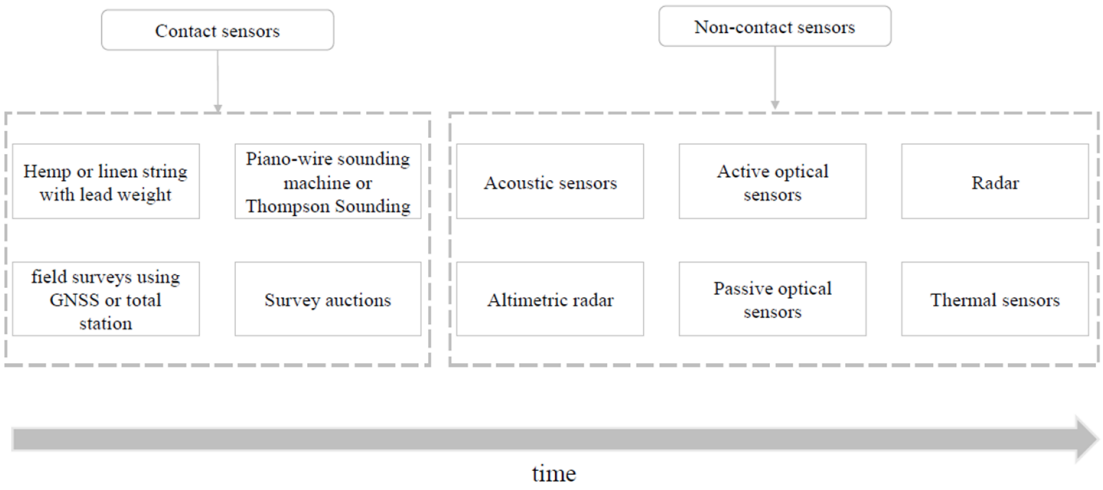

Figure 2. Classification of measurement sensors for bathymetric data acquisition.

In the mid-nineteenth century, bathymetric measurements were performed using contact-based point sensors. Although these instruments played a foundational role in the early development of seafloor exploration, they were inherently slow, spatially discontinuous, and susceptible to inaccuracies arising from external factors such as the influence of marine currents [32].

A major technological transition occurred in the 1920s with the introduction of acoustic sensors, which enabled non-contact direct depth measurements based on the propagation and reflection of sound waves [32]. The evolution of non-contact techniques accelerated markedly during the 1990s, with the emergence of sensors exploiting distinct physical principles, most notably optical systems relying on electromagnetic radiation and radar systems employing radio waves. These advances facilitated faster, more continuous, and spatially extensive bathymetric surveys, while significantly reducing the systematic errors associated with earlier methodologies.

In shallow-water environments, optical and radar sensors can also be employed to infer bathymetry by correlating wave characteristics, particularly those of wind-generated waves, with seabed morphology [33]; however, these are not the only waves observed in the data. The integration of multiple non-contact approaches enables coastal areas to be mapped under a broader range of environmental conditions, thereby improving the characterization of marine zones of high operational and scientific relevance [34].

Non-contact sensors may be deployed on platforms positioned at distances ranging from a few meters to several hundred kilometers, depending on the sensing technology and the objectives of the survey [35]. As platform distance from the seabed increases, the spatial extent of the surveyed area expands, whereas both spatial (Figure 3) and temporal resolution decrease. Consequently, for a given area of interest, sampling times are longer for techniques employing platforms located closer to the seabed.

 doi:10.20944/preprints202606.0385.v1

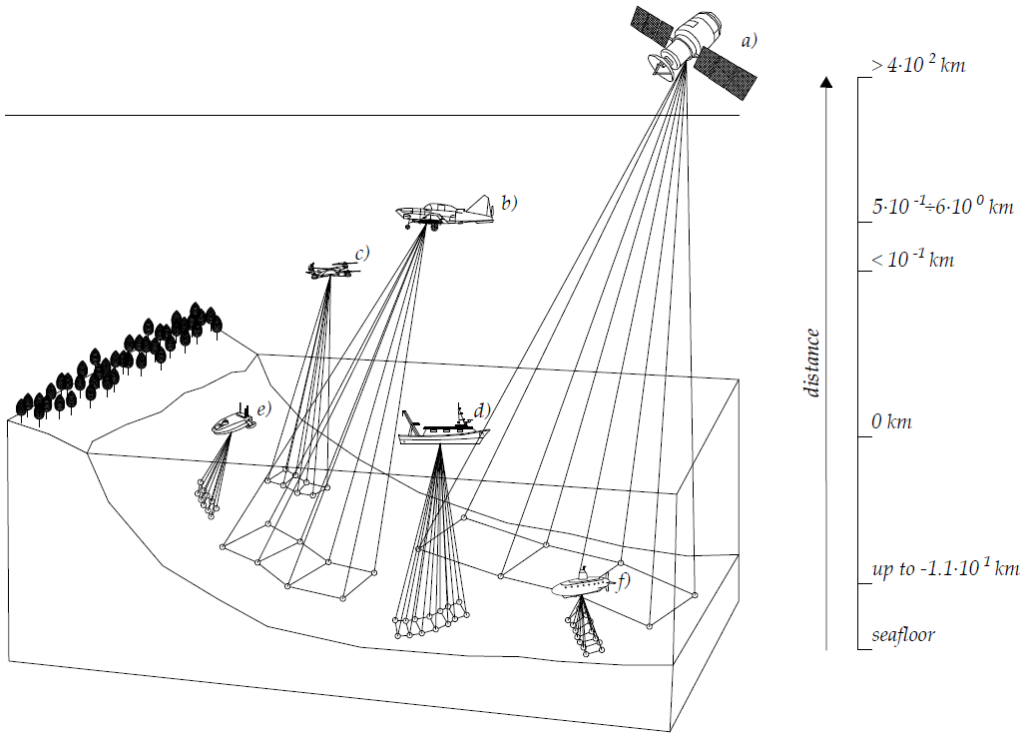

Figure 3. The sensor-seafloor distance, the surveyed area, and the source footprint. Platforms: (a) satellite; (b) aircraft; (c) drone; (d) surface vessel; (e) autonomous surface vehicle; (f) autonomous underwater vehicle.

The selection of the most appropriate platform for a given application must also account for logistical considerations, including operational costs, the accessibility of the survey area, and the potential requirement for specialized personnel (Table 4) [36,37].

Table 4. Cost, area accessibility, and the need for specialized personnel.

Platform	Operating Costs	Area Access	Need for Specialized Personnel
Satellite	Low	Global	Low
Aircraft	High	Wide, but subject to restrictions	High
Drone	Medium	High, even in remote areas	Medium
Vessel	High	Limited, for safety reasons	High
Autonomous surface vehicle	Medium	High, even in remote areas	Medium
Autonomous underwater vehicle	High	High, even in remote areas	High

To identify the most effective solution, it is essential to have a comprehensive understanding of each technique, together with its operational advantages and limitations.

3. Acoustic Bathymetry

This section summarizes the main acoustic techniques used in bathymetric surveying, including single-beam, multibeam, and interferometric systems, and the principles behind depth measurement and uncertainty. It also outlines data processing steps (Section 3.1) and the key factors affecting accuracy and reliability (Section 3.2).

 doi:10.20944/preprints202606.0385.v1

The operating principle of acoustic sensors is based on the propagation of sound waves through the aquatic environment. Among these instruments, echo sounders represent the most widely used devices for bathymetric measurements. An echo sounder consists of a transceiver unit that generates the electrical pulse transmitted to the transducer [35]. During transmission, the transducer acts as a projector, converting the electrical pulse into acoustic waves that propagate through the water column by inducing vibrations in the medium due to its slight compressibility.

During propagation, the acoustic signal may undergo scattering caused by fish schools, submarines, wrecks, gas bubbles, algae, or other obstacles [38]. In the absence of significant interference, the signal reaches the seabed, where part of its energy is absorbed and part is reflected toward the echo sounder [39]. Upon reception, the transducer operates as a hydrophone, reconverting the returning acoustic wave into an electrical signal. This signal is then amplified, filtered, and digitized by the transceiver.

The digitized data are processed by the acquisition software, which associates each received signal with the two-way travel time (Time of Arrival, TOA) according to a predefined beam angle [35] (Figure 4).

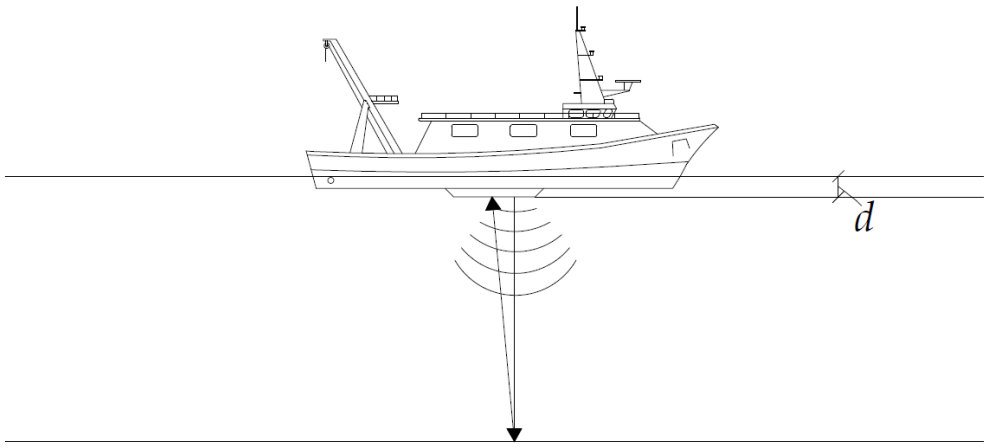

Figure 4. Schematic representation of a survey vessel equipped with an echo sounder system, with the draft d and the bathymetric depth as retrieved by an echo sounder system z_{EES}.

To convert the two-way travel time into a depth measurement, it is necessary to know the speed of sound in water. This parameter is not constant; rather, it varies spatially and temporally as a function of temperature, salinity, and pressure. For this reason, bathymetric surveys employ sound-velocity profilers or other instruments such as conductivity–temperature–depth probes, Expendable Bathythermograph or Moving Vessel Profilers, which allow the vertical profile of acoustic velocity along the water column to be measured [40,41].

Once the local sound speed and the TOA are known, the depth can be computed according to (1):

$$z^{EES} = \frac{v\,t}{2} + d \tag{1}$$

where z^{EES} (m) is the bathymetric depth as retrieved by an echo sounder system; v (m/s) is the sound speed, whose typical values are around 1500 m/s [42]; t (s) is the two-way travel time of the acoustic pulse; and d (m) is the draft, defined as the vertical distance between the transducer face and the static waterline. The determination of the static waterline is obtained through the integration of observations from tide gauges, which continuously record sea-level variations and provide an altimetric reference [43].

 doi:10.20944/preprints202606.0385.v1

A fundamental role is played by inertial measurement units (IMUs), which record the dynamic motions of the platform (roll, pitch, and yaw). Integrating inertial data makes it possible to compensate for the geometric distortions introduced by vessel motion, thereby improving the stability and reliability of the acoustic measurements [44].

Finally, to spatially position each depth value z, a pair of is assigned, allowing the three-dimensional location of every measured point to be defined. The determination of coordinates depends on the platform on which the sensor is installed. For echo sounders mounted on survey vessels or autonomous surface vehicles, spatial referencing is obtained through the integration of Global Navigation Satellite System (GNSS) and Inertial Navigation System data [45]. For autonomous underwater vehicles, positioning is generally estimated through Simultaneous Localization and Mapping procedures [46]. In high-resolution surveys, data are often acquired in a local reference system and subsequently georeferenced using ground-control points with known coordinates, ensuring geometric consistency and spatial accuracy in the generation of the final bathymetric model.

Echo sounders can be classified into single-beam echo sounders (SBES) and multibeam echo sounders (MBES). SBES, developed between the 1920s and 1930s, measure depth along a single vertical line beneath the vessel's keel. Technological advances between the 1950s and 1980s led to the development of MBES, which employ multiple acoustic beams arranged in a fan-shaped configuration, enabling the coverage of wide swaths of seafloor [47].

SBES are characterized by lower cost and simpler planning, deployment, and data processing. However, they require longer acquisition times, as multiple adjacent survey lines must be collected to cover large areas. Their cost-effectiveness makes them particularly suitable for small-scale surveys and shallow-water environments [47].

MBES, by contrast, involve higher costs and more complex data management and processing, requiring specialized personnel. Nevertheless, they significantly reduce acquisition time by covering broad areas in a single pass, with fields of view reaching up to 240°, while providing higher-resolution and more accurate data [48]. These characteristics make MBES particularly suitable for deep-water surveys and for large-scale mapping of complex seafloor morphologies [49].

As an alternative, depth can also be measured using echo sounders based on interferometric principles, known as Phase-Differencing Bathymetric Sonar (PDBS). This acquisition mode differs from the previous ones in that it employs multiple hydrophones arranged in an array (Figure 5).

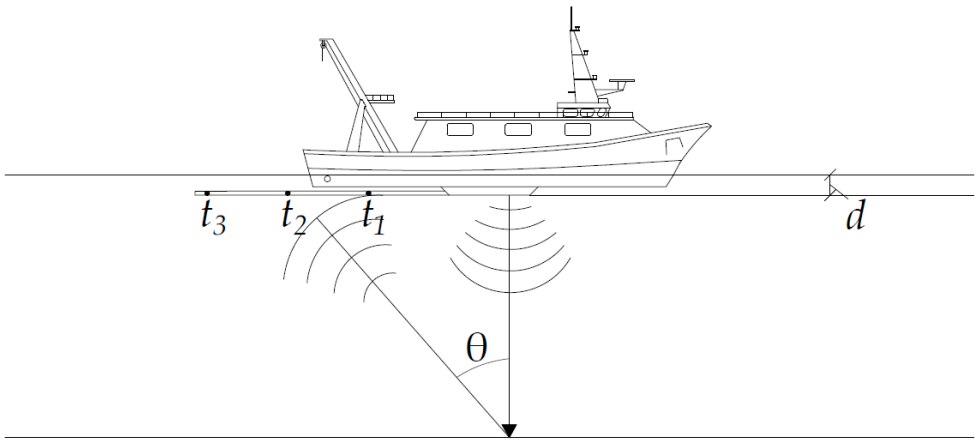

Figure 5. Schematic representation of a survey vessel equipped with a Phase Differencing Bathymetric Sonar. Where draft d and the bathymetric depth, θ(rad) is the angle of arrival of the reflected signal, and t_1,t_2,t_3 indicate the arrival times of the echo from the seabed at the different hydrophones.

 doi:10.20944/preprints202606.0385.v1

Because the seabed echo reaches each hydrophone at slightly different times, the system can measure the phase shift between the received signals and generate interference fringes. The analysis of these fringes allows the direction of arrival of the reflected signal to be determined. By combining the angle information with the two-way travel time and the sound speed in water, the bathymetric depth can be derived by a PDBS [50,51], according to (2):

$$z^{PDBS} = \frac{v\,t}{2} cos\theta + d \quad (2)$$

where z^{PDBS} (m) is the bathymetric depth retrieved by a PDBS, θ(rad) is the angle of arrival of the reflected signal.

Interferometric echo sounders, compared with time-of-flight systems, offer wider angular coverage, which increases survey productivity, particularly in shallow waters, while generally involving lower costs than other solutions. However, these systems also exhibit certain limitations: they provide lower point-wise accuracy, require higher computational resources, and are characterized by a blind zone at nadir (the nadir gap) [51]. Alongside echo sounders, other acoustic instruments have been developed for different purposes. Side-scan sonar (SSS) [52,53], for example, is used to obtain high-resolution two-dimensional images of the seafloor surface, enabling the detection of subtle morphological changes or the identification of objects that contrast with the surrounding substrate. Another instrument is the sub-bottom profiler [54], which, being positioned below the water surface, allows for the investigation of sedimentary layers beneath the seabed surface. Unlike echo sounders, these systems do not directly estimate water-column depth; instead, they provide complementary information that is essential for the morphological and geological characterization of marine environments.

3.1. Principles of Acoustic Bathymetry Processing

The processing of raw acoustic data is a critical step in the generation of bathymetric maps and involves a sequence of correction, filtering, interpolation, and validation procedures.

The workflow begins with the correction of the echo-sounder TOA to remove distortions caused by environmental, instrumental, and platform-motion [55]. These corrections rely on auxiliary observations collected during the survey, including sound-velocity profiles, tidal records, and inertial measurements from IMU/GNSS-INS systems [55–57]. Notably, Nadzir and Munthe (2025) [57] provide correction procedures for multibeam data that comply with current IHO standards.

The subsequent filtering phase reduces data redundancy while preserving the dataset's statistical representativeness [58]. Historically, this step relied on manual identification of outliers, a time-consuming task that often exceeded the duration of the survey itself [59]. Modern approaches, however, enable more efficient and automated data reduction. Common techniques include:

Grid reduction, which partitions the data into predefined cells and assigns each cell a representative value (mean, median, or mode) [60];

Clustering, which groups points based on spatial proximity or depth and selects a representative point for each cluster [61];

Geometric generalization algorithms, which remove redundant points while retaining those with the greatest deviation from reference polylines such as isobaths [58,62];

Self-Organizing Maps (SOM), which project the dataset onto a two-dimensional neural grid, enabling data reduction while preserving key morphological features of the seabed [63];

Hybrid approaches, such as the combination of SOM-based reduction (True bathymetric data reduction method) and generalization algorithms (e.g., Optimum Dataset), which allow flexible levels of reduction depending on local seabed complexity [64].

Interpolation follows, transforming discrete depth measurements into a continuous surface by estimating values in unsampled areas [65,66]. This step exploits spatial autocorrelation, whereby nearby points tend to exhibit similar depths [67,68]. In multibeam surveys, interpolation is mainly used to fill residual gaps, as acoustic swaths typically ensure near-complete coverage [40,69]. In

 doi:10.20944/preprints202606.0385.v1

contrast, single-beam surveys rely heavily on interpolation due to the sparse and irregular distribution of measurements [67].

The final step is *validation*, which assesses the accuracy and reliability of the bathymetric surface in accordance with the IHO S-44 standard. As summarized by Nadzir and Munthe (2025) [57], the standard defines four accuracy orders based on depth range, required coverage, and allowable vertical tolerance (Table 5).

Table 5. Accuracy thresholds established by the international IHO S-44 standard, which defines four orders of survey quality based on depth range, required seafloor coverage, and allowable vertical and horizontal uncertainty. Adapted from Nadzir and Munthe (2025) [57].

Order	Survey coverage (%)	Depth z (m)	Vertical tolerance, TVU (m)	Notes
Special Order	100	0 – 40	± 2 m	Critical areas (e.g., ports)
Order 1a	100	0 – 100	± (5 m + 5% · z)	Areas with high requirements
Order 1b	< 100	0 – 100	± (5 m + 5% · z)	Partial coverage
Order 2	< 100	> 100	± (20 m + 10% · z)	Greater depths

3.2. Factors Influencing Measurement Reliability

Echo-sounder measurements are shaped by the interplay between instrument-specific parameters and the environmental conditions during acquisition. These factors influence data reliability and determine whether the resulting bathymetry is suitable for a given application or not.

The depth ranges that can be effectively surveyed depend on sound-wave absorption within the water column and on the duration of the acoustic pulse (or ping) [39]. For a given operating frequency, signal absorption increases with depth, progressively reducing vertical discrimination. Conversely, at constant depths, higher frequencies attenuate more rapidly because their shorter wavelengths interact more strongly with the medium. Shorter pulse durations further enhance vertical resolution, enabling finer detection of seabed features.

Echo sounders typically operate across a broad frequency spectrum, from 12 kHz to 710 kHz (corresponding to wavelengths of roughly 125 mm to 2 mm) [70]. This range allows different tradeoffs between resolution, penetration, and accuracy, supporting a variety of applications and depth intervals [35]:

- 12–50 kHz: suitable for depths exceeding 1500 m;
- 50–200 kHz: used for depths between 200 m and 1500 m;
- >200 kHz: used for depths shallower than 200 m.

While Hodúl et al. (2018) [71] highlight that echo sounders are generally not deployed in coastal waters shallower than 4 m.

In this context, *multifrequency systems* offer a compromise between range, beamwidth, and accuracy [40], making them advantageous when surveys must span multiple depth zones with varying detail requirements.

Spatial resolution is governed by platform speed and sampling interval [72]. Reducing vessel speed or increasing sampling frequency increases data density and improves seabed representation. Water depth and acoustic beamwidth also influence the size of the insonified footprint: at constant depth, wider beams enlarge the footprint and reduce spatial resolution; at constant beamwidth, increasing depth has the same effect. Brandt and Lehmann (2025) [73] report minimum achievable resolutions of 9–35 cm at 10 m depth.

Measurement accuracy is affected by several factors, including instrument performance, operating frequency, and the assumptions embedded in processing models [40,55]. A common source of error is the assumption of constant sound speed in the water column. As shown by Menna et al.

 doi:10.20944/preprints202606.0385.v1

(2018) [70], a temperature change of just 1 °C increases sound speed by 4.6 m/s at 0 °C and by 2.5 m/s at 21 °C. Accurate bathymetry, therefore, requires sound-velocity profiling.

Sampling frequency also plays a key role. Higher frequencies improve resolution and thus accuracy but reduce penetration depth [39]. Lower frequencies penetrate further but may introduce uncertainties in specific environments. For example, in shallow waters, low-frequency signals may overestimate depth because they penetrate unconsolidated sediments and return echoes from deeper layers [35].

Given the several interacting factors, defining accuracy a priori is challenging. Ferreira et al. (2022) [35] provide a detailed assessment of uncertainty, closely linked to accuracy, as reducing uncertainty improves measurement reliability across different echo-sounder models, depths, and operating frequencies. Their results show, for instance, that a 200 kHz single-beam system typically exhibits a vertical uncertainty of about 1 cm ± 0.1% of measured depth, whereas a 200 kHz multibeam system can achieve uncertainties on the order of 1 mm.

Within this framework, acoustic systems remain applicable across the full depth spectrum: operational constraints may limit their use in shallow waters of few metres, while suitable frequencies allow echo sounders to reach several thousand metres. Multibeam sonars ensure high-resolution mapping even at great depths, whereas interferometric systems provide enhanced swath coverage and efficiency in shallow environments.

4. Optical Bathymetry

This section outlines optical bathymetric techniques, focusing on passive sensing and airborne LiDAR in shallow, clear waters. It highlights key principles, including light attenuation and water-column effects, and introduces passive methods (Section 4.1) and LiDAR (Section 4.2). A joint subsection addresses data processing and factors affecting reliability, defining the conditions and limitations of optical depth estimation.

The bathymetry estimation from optical data relies on the propagation of electromagnetic radiation within the visible spectrum (455–750 nm). As light travels through the water column, it undergoes absorption, scattering, and backscattering due to interactions with optically active substances. The properties of these particles, such as their size, shape, and chromatic composition, produce wavelength-dependent attenuation, which alters the intensity of the signal detected by the sensor and ultimately affects data quality [74].

Optical sensors can be broadly categorized as passive or active, depending on the source of radiation. Passive sensors working in the visible spectrum measure radiation reflected by surfaces, according to their reflectance characteristic. Among the most advanced passive approaches are spectrally derived bathymetry and photogrammetry [75]. Active sensors, in contrast, emit electromagnetic radiation toward the target and record the reflected return. A well-established example of this class is Airborne LiDAR Bathymetry (ALB).

4.1. Passive Optical Bathymetry

This subsection introduces passive optical bathymetry, explaining how sunlight interactions with the water column and seafloor can be used to infer depth. It outlines key principles such as light attenuation, water properties, and bottom reflectance, and presents radiometric and photogrammetric approaches. It also highlights sensor types, processing methods, and the main conditions and limitations affecting reliability.

Bathymetric measurements derived from passive optical sensors can be acquired using standard digital cameras equipped with RGB detectors or with radiometric multispectral or hyperspectral sensors [75]. Hyperspectral imaging generally offers superior performance due to its higher spectral resolution and the larger number of available bands at suitable wavelengths [76].

Depending on the platform on which they are mounted, RGB cameras may provide either an external or an underwater view of the scene. Underwater imaging requires the use of dedicated submersible digital cameras, typically operable down to approximately 15 m, or standard digital

 doi:10.20944/preprints202606.0385.v1

cameras housed in waterproof enclosures, which allow operations at greater depths [70]. These systems offer advantages in terms of portability, lens interchangeability, and lower cost. However, they are prone to lens aberrations, making geometric calibration necessary; in addition, when consumer-grade cameras are used (compact, DSLR/mirrorless, smartphones), radiometric calibration is also required [77].

Multispectral and hyperspectral cameras, by contrast, provide multiple spectral channels, even hundreds in the case of hyperspectral systems, greatly enhancing the ability to discriminate subtle variations in the recorded signal and improving bathymetric retrieval [78]. These benefits, however, come at a significantly higher cost and lower spatial resolution.

Bathymetric information extracted from imagery acquired by passive optical sensors can be obtained through *radiometric* or *photogrammetric* approaches.

4.1.1. Principles of Data Processing for Radiometric Derived Bathymetry

The radiometric approach is based on the inverse relationship between recorded electromagnetic radiation and water depth. Spectral sensors typically provide the most informative measurements in the blue and green regions of the spectrum (455–577 nm), where light attenuation in the water column is lowest, while the red, red-edge and near infrared components exhibit lower and wavelength-decreasing water column penetration [76,79].

This relationship can be described through radiative transfer models that represent, with varying degrees of complexity, the physical processes governing the propagation of electromagnetic radiation in the water column. In particular, the spectral radiance measured by the sensor can be expressed as the combined contribution of atmospheric, surface, water-column, and bottom interactions. Legleiter et al. (2009) [80] formalized this relationship in terms of radiance; expressed in terms of reflectance, it can be written as Equation (3). This formulation represents a conceptual simplification of the air–water radiative transfer, rigorously described by the radiative transfer equations of Chandrasekhar (1950) [81] for the atmosphere and Preisendorfer (1961) [82] for aquatic environments, linked through boundary conditions at the water surface that govern reflection and transmission between the two optical domains [83] (3):

$$R_T(\lambda) = R_B(\lambda) + R_C(\lambda) + R_S(\lambda) + R_P(\lambda) \quad (3)$$

where:

- $R_T(\lambda)$ *(-)* is the total reflectance recorded by the sensor,
- $R_B(\lambda)$ *(-)* is the bottom reflectance (some typical values are goe given by Legleiter et al., 2009) [84],
- $R_C(\lambda)$ *(-)* is the water-column reflectance,
- $R_S(\lambda)$ *(-)* is the surface-reflected component,
- $R_P(\lambda)$ *(-)* is the atmospheric direct and diffuse reflectance.

The reflectances $R_C(\lambda)$, $R_S(\lambda)$, and $R_P(\lambda)$ are estimated through atmospheric, surface, and water-column corrections, allowing isolation of the portion of the signal directly related to depth. The term $R_B(\lambda)$ representing bottom reflectance, it depends on the optical and physical properties of the substrate [85].

Following the Lambert–Beer law, Philpot (1989) [86] formalized a physically based relationship between bottom reflectance and depth in optically homogeneous waters (Equation 4), governed by the exponential decay of light with depth (4):

$$R^{(0^-)}(\lambda) = R_\infty(\lambda) + [R_B(\lambda) - R_\infty(\lambda)]e^{-2k_d(\lambda)z^R} \quad (4)$$

where:

- $R^{(0^-)}(\lambda)$ *(-)* is the reflectance just-below-surface,
- $R_\infty(\lambda)$ *(-)* is the infinitely deep-water reflectance (i.e., when the bottom does not contribute),
- $k_d(\lambda)$ *(1/m)* is the diffuse attenuation coefficient,

 doi:10.20944/preprints202606.0385.v1

- $z^R\ (m)$ is the bathymetric depth retrieved by radiometric data. The factor 2 accounts for attenuation along both the downward (surface–bottom) and upward (bottom–surface) optical paths.

Inverting Equation (4) yields depth as:

$$z^R = -\frac{1}{2k_d(\lambda)} ln\left(\frac{R^{(0^-)}(\lambda) - R_\infty(\lambda)}{R_B(\lambda) - R_\infty(\lambda)}\right) \quad (5)$$

The diffuse attenuation coefficient $k_d(\lambda)$ is an apparent optical property that varies widely across regions [87]. It describes the rate at which reflectance decreases along the optical path and is influenced by optically active substances, intrinsic optical properties of the water, and surface illumination conditions such as solar zenith angle and sea-surface state [88–90]. It can be estimated through in situ measurements of vertical reflectance profiles, empirical or semi-empirical remote-sensing algorithms, or neural-network models capable of learning nonlinear relationships between optical properties and environmental variables [89].

Typical values in blue wavelengths (at 490 nm) range from $k_d(490) < 0.25\text{m}^{-1}$ in oligotrophic ocean waters to $k_d(490) > 1\ \text{m}^{-1}$ in turbid coastal waters.

Building on the physically based formulation (Equation 4), semi-theoretical, semi-empirical, and data-driven inversion models have been developed since purely theoretical models require numerous physical and optical parameters that are difficult to measure directly in operational settings [76].

Semi-theoretical inversion models combine radiative-transfer theory with empirical relationships derived from calibration data [76]. Among semi-empirical models, the most widely used are the *log-ratio* and *multiband regression* approaches, which serve as benchmarks for accuracy assessment [5].

Log-ratio model [91]

$$z^R = m_1 \frac{ln\ (l\ R_b)}{ln\ (l\ R_g)} - m_0 \quad (6)$$

where:

- m_1 (-) is a scaling constant,
- $m_0\ (m)$ is an offset corresponding to $z = 0$,
- l (-) is an empirical constant,
- R_b (-) and R_g (-) are reflectances in the blue and green bands. The parameters $m_1$and m_0 are derived by calibration.

Multiband regression model [92,93]

$$z^R = h_0 + \sum_{i=1}^{n} h_i\ ln\ (R_i - R_\infty) \quad (7)$$

where:

- h_0 and h_i (m) are empirical coefficients estimated by calibration depths,
- R_i (-) is the reflectance in band i, corrected for atmospheric effects and sun-glint,

Nocera et al. *2026* model [94]:

$$ln\left(\langle R^{(0^-)}\rangle - R_\infty\right) = ln(R_B - R_\infty) - 2m_{K_d} z^{R^2} - 2q_{K_d} z^R \quad (8)$$

Where the k_d is assumed to vary linearly with depth:

- m_{Kd} (1/m²) quantifies the rate of change of k_d per unit depth (i.e., the slope of the Kd(z) relationship),
- q_{Kd} (1/m) represents the value of k_d at the depth where the water column approaches zero (i.e., the intercept of the $k_d(z)$ relationship),
- $\langle R^{(0^-)}\rangle$ (-) is the reflectance just below the surface, averaged over the spectrum and time.

 doi:10.20944/preprints202606.0385.v1

Statistical and data-driven models

These approaches do not explicitly model optical physics but instead identify empirical, often nonlinear, relationships between spectral reflectance and depth, based on calibration data [95]. Common examples include Principal Component Analysis (PCA) and Artificial Neural Networks (ANNs).

PCA transforms correlated spectral bands into independent components. The first principal component (PC1), which captures most of the spectral variance, is typically the most strongly correlated with depth. A linear regression between PC1 and calibration depths is then used to estimate bathymetry [96].

ANNs consist of interconnected nodes arranged in input, hidden, and output layers. The input layer receives spectral reflectances, hidden layers apply nonlinear activation functions weighted by trainable parameters, and the output layer produces the estimated depth. The network iteratively adjusts its weights through backpropagation to minimize the error between predicted and observed depths [97]:

$$z^R{}_{ANNs} = \frac{\sum_{i=1}^{k}\left(\frac{z_i}{1-p_{FMVi}}\right)}{\sum_{i=1}^{k}\left(\frac{1}{1-p_{FMVi}}\right)} \quad (9)$$

where:

- $z^R{}_{ANNs}\ (m)$ is the estimated depth,
- z_i (m) are depth of training points,
- p_{FMVi} (-) is the probability associated with the point, obtained by Fuzzy Majority Voting [97].

4.1.2. Principles of Data Processing for Photogrammetric Derived Bathymetry

The photogrammetric approach exploits the principles of optical imaging and projective geometry to reconstruct the three-dimensional coordinates of seafloor points from stereoscopic imagery. Accurate depth retrieval requires image pairs with substantial forward overlap, typically between 70% and 80%, to ensure robust tie-point extraction and reliable bundle adjustment [98].

In aquatic environments, bathymetry can be derived by combining the collinearity equations with Snell's law [99].

The collinearity equations [100] define the geometric relationship between the object point, the camera perspective center, and its corresponding image point.

The collinearity equation must be adapted to account for light refraction at the air–water interface. This phenomenon is governed by Snell's law [101], describing the change in propagation direction experienced by a light ray crossing two media (air and water) with different refractive indices (10, 11):

$$\theta_{w1} = sin^{-1}\left(\frac{\sin(\theta_{a1})}{n}\right) \quad (10)$$

$$\theta_{w2} = sin^{-1}\left(\frac{\sin(\theta_{a2})}{n}\right) \quad (11)$$

where:

- θ_{a1} and θ_{a2} (rad) are incidence angles, calculated from off-nadir angles of each
- θ_{w1} and θ_{w2} (rad) are the corresponding refraction angles in water.
- n *(-)* is the refractive index

 doi:10.20944/preprints202606.0385.v1

The magnitude of refraction depends on several water-column properties, including temperature, salinity, density, and suspended constituents, as well as on the incidence angle and the instantaneous roughness of the water surface [102].

If refraction is not explicitly corrected, causes the reconstructed depth to be systematically underestimated, leading to the so-called *apparent depth*, a well-known bias in underwater photogrammetry (Figure 6).

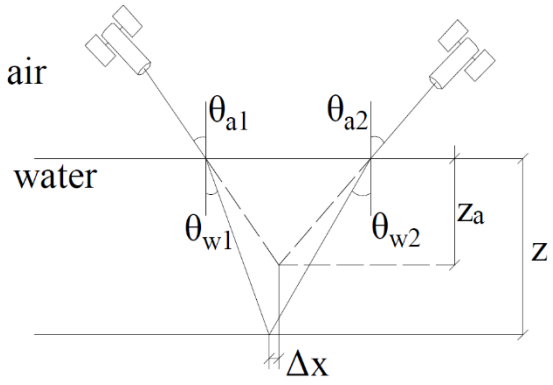

Figure 6. Light Refraction at a Air-Water Interface.

Although refraction also introduces a horizontal displacement, its magnitude is generally small and often negligible for most geomatic applications [103].

The refractive indices and light velocities relevant to bathymetric photogrammetric processing are summarized in Table 6.

Table 6. Refractive Indices and Light Velocities in Media Relevant to Bathymetric Photogrammetry.

Medium	Refractive index (-)	Speed of light (m/s)
Air	1.0003	2.999×10^8
Water	1.33	2.26×10^8
Glass	1.5 - 1.9	2.00×10^8

The reconstruction of bathymetry requires compensating for the geometric distortions introduced by light refraction at the air–water interface. When the water surface represents the only refractive boundary, the depth can be corrected using a two-medium model [99], as illustrated in Figure 6. Under this assumption, the relationship between the apparent depth and the true depth is expressed by (12):

The two-medium correction can be expressed as:

$$z^P = \frac{tan\ \theta_{a1} + tan\ \theta_{a2}}{tan\ \theta_{w1} + tan\ \theta_{w2}}\, z_a \tag{12}$$

where:

- $z^P\ (m)$ is the bathymetric depth retrieved by collinearity equations
- z_a(m) is the apparent depth derived from uncorrected photogrammetry.

Equation (12) is fully consistent with Snell's law and provides a physics-based correction that links the apparent geometry observed in the images to true underwater geometry. Its accuracy depends on the correct estimation of the incidence and refraction angles, which are governed by the refractive indices and light velocities of the media involved parameters discussed in the preceding section.

In more complex scenarios, a multi-medium correction becomes necessary. Under calm water conditions, this occurs when the water column exhibits stratification with varying refractive indices,

 doi:10.20944/preprints202606.0385.v1

typically due to temperature or salinity gradients [104] (Figure 7, panel a), or when the imaging system operates underwater and the camera is enclosed within a housing equipped with a flat or dome-shaped port (Figure 7, panel b). Dome ports generally ensure superior optical and photogrammetric performance, as demonstrated by Menna et al. [2017] [105], because they minimize refraction-induced distortions and preserve the validity of the collinearity model more effectively than flat ports.

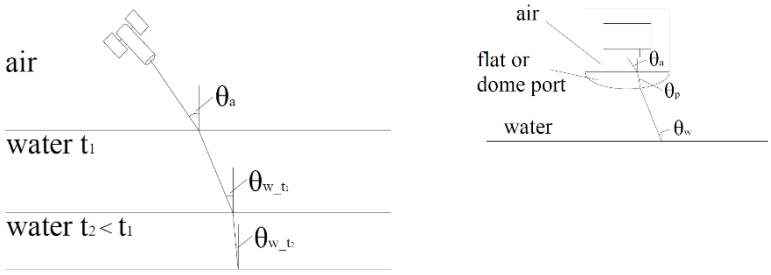

(a) (b)

Figure 7. Light refraction: (a) stratified water column with layers exhibiting different refractive indices; (b) underwater imaging system with the camera enclosed in a housing equipped with either a flat or dome-shaped port.

Beside physically based refraction models, geometric, empirical, and data-driven approaches have been proposed to correct apparent depths derived from photogrammetry. These methods provide alternative solutions when the physical properties of the water column are unknown, when environmental conditions complicate the application of multi-medium models, or when operational constraints require simplified correction strategies.

Woodget et al. [2015] [106] assume that for small incidence angles (<10°) Snell's law can be approximated linearly. Under this assumption, the true depth becomes directly proportional to the apparent depth according to Equation (13):

$$z^P = n_w \, z_a \tag{13}$$

where n_w(–) the refractive index of water.

Dietrich [2017] [107] introduces an iterative multi-camera approach. For each camera position, the horizontal distance and elevation difference relative to the target point are computed, allowing the incidence angle to be estimated. Snell's law is then applied to derive the corresponding refraction angle and the corrected depth for each camera viewpoint. The final depth is obtained by averaging the corrected values, as expressed in Equation (14):

$$z^P = z_{ws} - \bar{z} \tag{14}$$

where z_{ws}(m) is the water-surface elevation and $\bar{z}$(m) is the mean corrected depth derived from all cameras observing the point.

Partama [2017] [108] proposes an empirical linear-regression model that relates apparent depths to reference measurements acquired with independent sensors. The relationship is expressed as:

$$z^P = p \, z_a + \beta \tag{15}$$

where p(–) is an empirically derived correction factor and β(–) is an offset term, often set to zero.

Agrafiotis et al. [2019] [1] introduced machine-learning-based correction methods. In their work, Support Vector Regression models are trained using bathymetric LiDAR data as ground truth. Once calibrated, the model is applied to photogrammetrically derived depths in areas lacking direct measurements, enabling spatially consistent correction even in heterogeneous environments.

From an operational perspective, because the collinearity alone does not allow the reconstruction of underwater topography, depth retrieval requires homologous points identified in

 doi:10.20944/preprints202606.0385.v1

stereoscopic imagery and accurate knowledge of both interior and exterior orientation parameters. Interior orientation is obtained through camera calibration, while exterior orientation is typically determined using Ground Control Points (GCPs) [100,109]. When GCPs lie on dry land, standard photogrammetric procedures can be applied. However, when GCPs fall within the water body, their apparent positions are affected by refraction and must be corrected accordingly [104,109].

Advances in digital photogrammetry have also led to the widespread adoption of automated computer-vision workflows such as Structure-from-Motion (SfM) [110] and Dense Image Matching [111,112]. These techniques integrate camera calibration, orientation, and dense point-cloud generation within a unified pipeline using large sets of overlapping images. Refraction correction can be applied either as a post-processing step or integrated directly into the workflow [1,107,113], enabling an operationally efficient reconstruction of submerged topography.

Within this framework, optical bathymetry remains inherently constrained to shallow, optically clear waters. Radiometric approaches, including empirical multispectral methods and physics-based models**,** typically operate from the shoreline to a few tens of metres, with their effective depth range controlled by light penetration, water turbidity, and bottom reflectance. Photogrammetric techniques, which rely on geometric reconstruction rather than spectral response, exhibit similar depth limitations: although they can achieve high spatial detail in very clear waters, their performance rapidly degrades as water depth increases due to loss of image contrast and bottom visibility. Beyond these shallow ranges, increasing absorption and scattering severely restrict the applicability of all optical methods.

4.2. LiDAR Bathymetry

This subsection outlines active optical bathymetry, focusing on airborne LiDAR applications in shallow, relatively clear waters. It introduces laser–water interaction principles and key system characteristics, along with processing steps for extracting depth from return signals. It also summarizes factors affecting reliability and highlights the main conditions and limitations of LiDAR-based bathymetry.

4.2.1. Principles of LiDAR Bathymetry Processing

LiDAR systems measure depth by estimating the time-of-flight of a laser pulse, either directly (timing the return) or indirectly (comparing waveform shapes). The distance between the sensor and the target is obtained by multiplying the ToF by the speed of light and dividing by two (two-way travel path) [114].

In bathymetric applications, the interaction of the laser pulse with the air–water interface induces refraction (Section 4.1.2), altering both the propagation direction and velocity. As a result, the total travel time of the bottom return is the sum of the propagation times in air and in water (16):

$$T_b = T_s + T_w \tag{16}$$

where: T_b(s) is the total two-way travel time of the bottom return, T_s(s) is the two-way travel time of the surface return, and T_w(s) is the two-way travel time in water.

Because seawater is significantly denser than air, the speed of light in water is lower; therefore, for the same path length, T_w, is greater than T_s. If refraction is not accounted for, depth is systematically overestimated, producing an apparent depth larger than the true one [115].

By incorporating refraction into the ranging equation, under calm sea conditions, depth can be expressed as [116] (17):

$$z^{Li} = \frac{1}{2}\frac{c}{n_w} T_w cos\ \theta_w = \frac{1}{2}\frac{c}{n_w}(T_b - T_s) cos\ \theta_w \tag{17}$$

where: $z^{Li}\ (m)$ is the bathymetric depth retrieved by LiDAR data, c(m/s) is the speed of light in air, and θ_w(rad) is the refracted angle relative to the surface normal.

 doi:10.20944/preprints202606.0385.v1

Two main categories of bathymetric LiDAR systems are commonly used [117]: Dual-frequency Bathymetric LiDAR and Single-photon Bathymetric LiDAR.

Dual-frequency systems (Figure 8) emit a green or blue-green laser pulse (532 nm), used to measure the bottom return, T_b; and an infrared pulse (1064 nm), used to measure the surface return, T_s [117]. The sensor records the temporal evolution of the reflected optical intensity in two acquisition modes [118,119]: i) a discrete-return mode, in which only the times at which the received intensity exceeds a predefined threshold are stored; and a full-waveform mode, in which the complete temporal profile of the reflected signal is digitized. Each point of the waveform represents the cumulative contribution of reflections from the surface, water column, and seabed.

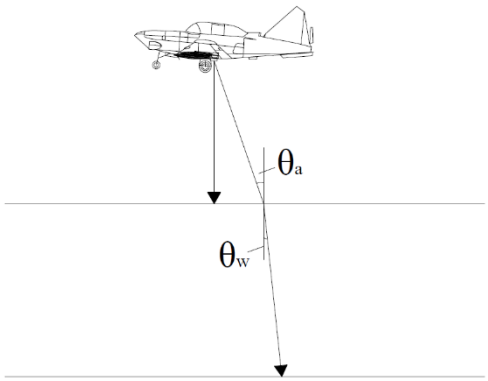

Figure 8. Schematic representation of ToF ranging.

The full-waveform (FWF) acquisition enables more effective discrimination between surface and bottom returns but is more sensitive to noise [120,121].

The FWF processing can be performed either in real time or during post-processing [122]. The procedure consists of decomposing the recorded optical signal to identify the individual returns associated with the water surface, water column, seafloor, and noise components (Figure 9).

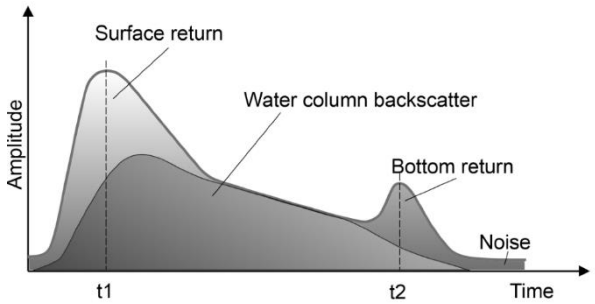

Figure 9. *LiDAR waveform. Adapted from He* et al., *2024* [78].

This decomposition enables a more accurate separation of overlapping echoes and improves the characterization of the bottom return, particularly in environments with strong turbidity or complex backscattering conditions.

Waveform-processing algorithms can be broadly classified into three main categories:

- the echo detection, which does not consider the radiometric properties of the targets but focuses solely on identifying echo positions through direct indicators such as an intensity threshold, the zero-crossing of the second derivative [123], or the Average Square Difference Function [124];
- the deconvolution, which aims to isolate the surface or bottom response by removing the transmitted-waveform component from the received signal. Representative methods include Wiener filter deconvolution [125] and Richardson–Lucy deconvolution [126];

 doi:10.20944/preprints202606.0385.v1

- the mathematical approximation, which fits analytical functions to the waveform to determine target locations. Gaussian decomposition is the most widely adopted approach, as approximately 98% of an echo signal can be represented by a combination of Gaussian curves [120]. Other functional forms, such as lognormal, Weibull [127], or quadrilateral functions [128], have also been explored to model the water-column response.

Single-photon bathymetric LiDAR represents a recent technological advancement compared to conventional multifrequency bathymetric systems. It employs high-frequency laser micro-pulses and detectors that are two to three orders of magnitude more sensitive than those used in traditional systems [129]. The technology is characterized by low weight and cost, high operational flexibility, and excellent vertical accuracy [121], although it is more susceptible to noise [130].

Operationally, the system emits a single green or blue-green laser pulse, from which information on both the water surface and the seabed is derived. The air–water interface is indirectly modeled from reflections in the green channel, based on photon counts recorded by the sensor [121,129]. The sensor measures the arrival time of the i-th photon, enabling the construction of a discrete histogram of photon density as a function of ToF. Because the number of photons reflected from the water surface is typically much higher than background noise and seabed returns, the maximum occurrence frequency provides a robust estimate of the surface ToF T_s [129]. To mitigate the presence of noise photons within the extracted surface layer, clustering and adaptive filtering techniques are commonly applied [129,131].

After isolating photons below the water surface, the most widely used method for estimating the seabed ToF T_b is density-based denoising, which assumes that seabed returns form spatially coherent clusters relative to noise photons [132]. For instance, Ma et al. (2020) [133] apply an adaptive threshold based on the minimum number of neighboring points within a given distance to distinguish valid photons from noise. A comprehensive overview of interface-discrimination and depth-retrieval techniques is provided by Jung et al. (2025) [131].

4.3. Factors Influencing Measurement Reliability

Bathymetric measurements derived from optical sensors are strongly influenced by the interaction between the instrument's parameters and the environmental conditions at the time of acquisition. These directly affect data reliability and determine the suitability of each technique for specific applications.

The range of depths that can be effectively surveyed depends on the intensity of the detected signal, which in turn is controlled by both sensor sensitivity and environmental characteristics. In LiDAR systems, the ability to discriminate the return signal is primarily governed by light attenuation within the water column, target-surface properties, acquisition geometry, sensor sensitivity, signal-to-noise ratio, and laserpulse duration, with short pulses enhancing the separation of closely spaced returns [134]. In passive optical systems, signal discrimination is mainly a function of water column light attenuation and illumination distribution [135].

In both acquisition modalities, the dominant physical process affecting measurement reliability is the wavelength-dependent attenuation of electromagnetic energy. The spectral bands with the greatest penetration capability are those in the blue and green regions (Sections 4.1 and 4.2). This behavior is controlled by the size, shape, and optical properties of optically active substances, including phytoplankton, non chlorophyllous particles, and colored dissolved organic matter (CDOM).

Phytoplankton and non chlorophyllous particles influence both absorption and scattering processes. Phytoplankton consists of unicellular algae; as its concentration increases, spectral reflectance in the blue region decreases, approaching values typical of the green band. Non chlorophyllous particles may be of organic origin (microorganisms, bacteria, viruses) or inorganic origin (silicates and carbonates of biological or terrestrial provenance). Increasing concentrations of these particles shift the reflectance peak toward the yellow–orange region. CDOM, which originates

 doi:10.20944/preprints202606.0385.v1

from the degradation of organic material such as phytoplankton, contributes exclusively to absorption processes within the water column.

Radiation attenuation is also directly related to the concentration of optically active substances: higher concentrations increase water column turbidity and enhance the attenuation of electromagnetic energy [74].

Optically active substances attenuate the intensity of the signal detected by both active and passive optical sensors according to an exponential decay law (4), thereby determining the maximum depth that can be effectively surveyed [74].

Two main operational categories of LiDAR systems can be distinguished [70]:

- Shallow water systems (<10 m), which employ lowerplower-powerpulses and higher measurement frequencies, resulting in finer spatial resolution;
- Deepwater systems (10–50 m), which use higher power pulses and lower measurement frequencies, leading to coarser spatial resolution.

The reported depth ranges should be regarded as indicative values applicable under clear-water conditions.

At depths shallower than 2 m, it becomes particularly challenging to separate the signal reflected by the seabed from that originating at the water surface [136].

For passive optical systems based on photogrammetric techniques, bathymetry can be retrieved down to approximately 20 m in clear waters [137]. For passive radiometric approaches, the operational depth range typically extends to 25–30 m [138], although these values should be regarded as indicative, as the effective penetration depth is strongly influenced by the spatial and temporal variability of optically active substances. For instance, in high-energy coastal environments characterized by elevated suspended sediment concentrations, radiometric passive systems are generally limited to depths between 0 and 6 m [138], whereas LiDAR systems may reach depths of up to 10 m [139].

Duplančić Leder et al. (2023b) [140] report depth ranges identified by Earth Observation and Mapping for the radiometric approach across different oceanographic settings: Red Sea (20–30 m), Gulf region (5–15 m from north to south), Mediterranean Sea (20–30 m), Baltic Sea (2–15 m from north to south), Caribbean Sea (20–30 m), U.S. West Coast (5–15 m), and the Pacific region (20–30 m).

The spatial resolution of optical systems is determined by acquisition geometry and sensor characteristics. In LiDAR systems, it is directly influenced by point cloud density [141], which depends on scanning frequency, platform speed, scanner field of view, and flight altitude. Increasing altitude allows larger areas to be covered but reduces point density and, consequently, spatial resolution [142]. In passive optical systems, spatial resolution corresponds to pixel size, which increases with sensor altitude, thereby reducing spatial detail [143].

The accuracy of bathymetric measurements derived from optical sensors is influenced by a combination of geometric, radiometric, and environmental factors, among which refraction is particularly critical. In passive photogrammetric systems, refraction at the water surface alters the propagation direction of the imaging rays, leading to depth underestimation (Section 4.1.2). In bathymetric LiDAR systems, refraction slows the speed of light in water and may result in depth overestimation (Section 4.2). Additional factors affecting accuracy in passive optical systems include sun glint, surface roughness, substrate reflectance properties [95], nonuniform illumination, and meteorological variability [135]. For radiometric techniques, the robustness of the model used to convert radiometric information into depth estimates plays a key role. In LiDAR systems, further sources of uncertainty include surface roughness [139], point cloud density [141], signal to noise ratio, and the correct separation of contributions from the surface, water column, seabed, and noise [120,121].

Typical vertical uncertainty for bathymetric LiDAR ranges between ±0.15 and ±0.30 m, while horizontal uncertainty generally falls between ±2.5 m and ±3.5 m [49]. For passive radiometric systems, vertical uncertainty is typically below 5% of the maximum depth, with values on the order

 doi:10.20944/preprints202606.0385.v1

of ±0.5 to ±1.3 m [144]. Finally, for passive photogrammetric systems, mean vertical uncertainty is approximately ±2 m within the 5–20 m depth range [78].

5. Wave Spectrum Bathymetry

This section outlines wave-spectrum methods for bathymetry retrieval based on wave propagation over varying seafloor topography. It highlights the link between wave properties and water depth, summarizes data processing (Section 5.1), and identifies key environmental factors affecting accuracy. These elements define the potential and limitations of this approach, especially in shallow, dynamic coastal areas.

In this context, both coastal X-band radars have been employed for high-resolution monitoring [145], as well as C-band SAR sensors [146].

The Wave Spectrum Bathymetric (WSB) method provides an indirect approach to estimating bathymetry by analyzing wave spectrum. These spectra can be extracted from synthetic aperture radar (SAR) imagery, passive optical imagery, or even coastal video photogrammetry, allowing bathymetric information to be inferred from the pattern of surface waves [78].

The method is based on the analysis of wave propagation in shallow and intermediate waters, defined respectively by a bathymetric depth, z(m), to wavelength, L(m), ratio smaller than 1/20, and by 1/20 < z/L < 1/2 [147]. Under these conditions, wave propagation is modulated by water depth [148], which governs processes such as shoaling and refraction. Shoaling leads to wave steepening, characterized by increasing wave height and decreasing wavelength, whereas refraction induces a rotation of the wavefront as waves propagate over variable bathymetry [149,150].

From a mathematical perspective, the propagation of surface waves is described by the dispersion relation [151], Equation (18):

$$(2\pi f)^2 = gktanh\,(kz^{WSB}) \tag{18}$$

Where z^{WSB} (m) is the bathymetric depth retrieved by WSB, f (1/s) is the wave frequency; g (m/s²) is gravitational acceleration; and $k = 2\pi/L$ (1/m) is the wavenumber.

Wave spectrum analysis enables the extraction of the main wave characteristics from imagery by applying a two dimensional Discrete Fourier Transform [152]. This transformation converts the spatial (or temporal) intensity representation into the frequency domain [153], from which the dominant wavelength (19), L, and propagation direction (20), θ (rad), can be quantified by the peak of maximum spectral intensity [27]:

$$L = \frac{2\pi}{k} = \frac{2\pi}{\sqrt{k_x^2 + k_y^2}} \tag{19}$$

where k_x and k_y (1/m) are the wavenumbers in the x and y directions, respectively.

$$\theta_{dir} = arctan\left(\frac{k_y}{k_x}\right) \tag{20}$$

where θ_{dir} (rad) is the dominant wave direction.

5.1. Principles of Wave Spectrum Bathymetry Processing

In passive optical remote sensing imagery, the observed signal is radiometric in nature, and pixel intensity represents radiance or reflectance in a specific spectral band. Wave patterns become visible through the Sun Glint effect, generated by the specular reflection of solar radiation on the slopes of surface waves [154], producing pixels with higher reflectance values. The reflection depends on the relative geometry between the sensor, the wave propagation direction, the solar azimuth, and the solar elevation angle [154]. Under fixed acquisition geometry, radiometric variations are correlated with the slope and elevation of the water surface [155]. The Near Infrared band is particularly effective for wave studies because radiation in this range is strongly absorbed by water, and the

 doi:10.20944/preprints202606.0385.v1

observed radiometric signal contains information exclusively from the water surface layer, with minimal influence from water column optical properties [156].

In SAR imagery, pixel intensity represents the radar backscatter coefficient, which depends on the geometric and dielectric properties of the sea surface. Increased surface roughness, typically associated with rougher sea states, produces higher radar backscatter, appearing as brighter regions in SAR images. Consequently, SAR imagery displays alternating areas of high and low backscatter corresponding to wavefront positions [138]. Radar backscatter from the ocean surface is commonly described using a two scale scattering model combining the Kirchhoff model, applicable to largescale undulations and low incidence angles (≈ 0°–20°), and the Bragg model, dominant for small scale roughness and intermediate to high incidence angles (≈ 20°–70°) [157]. Since spaceborne SAR sensors typically operate within this latter range, Bragg scattering represents the primary contribution to the observed backscatter [157,158]. Applying the WSB method to SAR data also requires knowledge of environmental conditions, particularly wind fields and tidal currents, as wind speed and direction influence the generation and modulation of surface roughness, affecting radar backscatter. This contribution must be estimated and removed to isolate the modulation associated with wavefronts, also in frequent conditions characterized by the coexistence of long waves (swell) and wind-generated waves.

Operationally, the analysis begins with the wavenumber spectrum of the dominant wave in deep water, allowing the determination of the wavenumber k [27]. Since the dispersion equation in deep water is independent of depth (21), the wave frequency (thus the period) can be derived and assumed constant during propagation, as it depends on the forcing mechanism generating the wave [151]:

$$(2\pi f)^2 = gk \tag{21}$$

Subsequently, the wavenumber spectrum of the dominant wave in shallow water is analyzed to estimate the new value of k. Given the frequency and the shallow water wavenumber, the general dispersion equation (18) can be inverted [159] to derive bathymetry (22):

$$z^{WSB} = \frac{1}{k} arctanh\left(\frac{(2\pi f)^2}{gk}\right) \tag{22}$$

Alternatively, for video or imagery acquired with short temporal intervals, wave celerity can be estimated (23). Combined with the dominant wavenumber spectrum, this enables bathymetry retrieval in intermediate and shallow waters (24) [147]:

$$C^2 = \frac{g}{k} tanh\,(kz^{WSB}) \tag{23}$$

where C (m/s) is wave celerity.

$$z^{WSB} = \frac{1}{k} arctanh\left(\frac{C^2 k}{g}\right) \tag{24}$$

For waves with significant height greater than ≈1 m and under fixed sun–wave–sensor geometry, ideally, wave propagation does not involve net horizontal mass transport but only the propagation of the wave form. Consequently, Sun Glint reflections remain tied to instantaneous surface slopes and move with the wave [158]. This displacement can be observed in image sequences or video products. In multispectral satellite imagery (e.g., Sentinel-2, SPOT, Pleiades), different spectral bands are acquired at slightly different times, resulting in a known temporal offset between bands [147]. Similarly, a video can be interpreted as a dataset composed of multiple frames acquired over a specific time interval [155].

Thus, when imagery is acquired with a known temporal interval, wave celerity can be estimated using a space–time cross–correlation approach applied to pairs of images or consecutive video frames. The maximum of the cross correlation function identifies the most probable displacement of the wavefront, from which phase celerity can be derived, given the temporal delay between images [153,155,158].

 doi:10.20944/preprints202606.0385.v1

5.2. Factors Influencing Measurement Reliability

The accuracy of bathymetric estimates obtained through WSB arises from the interplay between wave characteristics, environmental conditions, and sensor- and processing related parameters. Understanding these factors allows delineating the operational limits of the method and interpreting its performance across diverse coastal settings.

A primary constraint on WSB accuracy is the wavelength of the observed waves, which governs the maximum depth at which dispersion effects are detectable: i) long waves enable the retrieval of deeper bathymetry, while ii) short waves restrict the method to shallow water.

Shallow, intermediate, and deep water definitions are wavelength dependent (Section 5). The significant wave height is equally critical: in SAR systems, waves with $H_s < 1.4$ m are typically not detectable [160], limiting the extraction of a correct wave spectrum.

The seabed slope further modulates the depth range: steeper bathymetries enhance the sensitivity of the wavenumber–depth relationship, whereas gentle slopes reduce the observable variation in wavenumber. Consequently, the maximum retrievable depth is site specific, controlled by: i) the dominant wavelength; ii) the forcing factors that generated the wave field; and iii) the seabed morphology.

Reported values typically reach 50–60 m [153] and may extend to 100–200 m in areas with pronounced seabed gradients [161].

Spatial resolution is governed by the acquisition geometry, particularly the sensor–surface distance, and by the size of the analysis windows used for the two dimensional Fourier transform. Larger windows improve the stability of the dominant wavenumber estimate but reduce spatial detail, requiring a balance between spectral robustness and cartographic resolution [147].

WSB accuracy is influenced by both theoretical assumptions and sensor specific limitations. The method relies on the assumption of linear wave propagation, a simplification that may introduce errors under nonlinear conditions, wave–current interactions, or complex sea states [151].

For optical imagery, accuracy depends on the visibility of wave patterns, which is strongly affected by the sun–wave–sensor geometry, thus, the occurrence of Sun Glint; and the atmospheric conditions such as cloud cover or haze. These factors, indeed, diminish the radiometric contrast of wave slopes, thus reducing the quality of the extracted spectrum [155,156].

In SAR imagery, accuracy is controlled by radar backscattering, including the wind induced surface roughness responsible for Bragg scattering. Variations in wind speed and the presence of tidal currents may obscure the wave signal, making the estimation and removal of the wind contribution a main source of uncertainty [27].

Concluding, the accuracy of WSB cannot be defined a priori, as it depends on sea state, sensor characteristics, and processing strategies. Indicative values are mean error: 18% ± 0.3–47%, with the highest accuracy reached at ≈12 m depth [27].

Within this framework, wave-spectrum bathymetry is inherently restricted to shallow, wave-dominated coastal environments, where wave transformation is strongly controlled by seafloor morphology. These approaches are typically effective from the shoreline to depths of a few tens of metres, beyond which wave dispersion becomes increasingly insensitive to bottom topography, thereby limiting the applicability of wave-based inversion techniques.

6. Radar–Altimetric Bathymetry

This section outlines radar-altimetric bathymetry, explaining how satellite measurements of sea-surface height relate to seafloor topography. It summarizes key principles, signal corrections (Section 6.1), and the use of geoid and gravity variations to infer large-scale structures, highlighting the method's strengths and limitations.

Radar altimeters operate by transmitting microwave pulses toward the ocean surface and measuring ToF between the satellite and the sea surface, as schematically illustrated in Figure 10.

 doi:10.20944/preprints202606.0385.v1

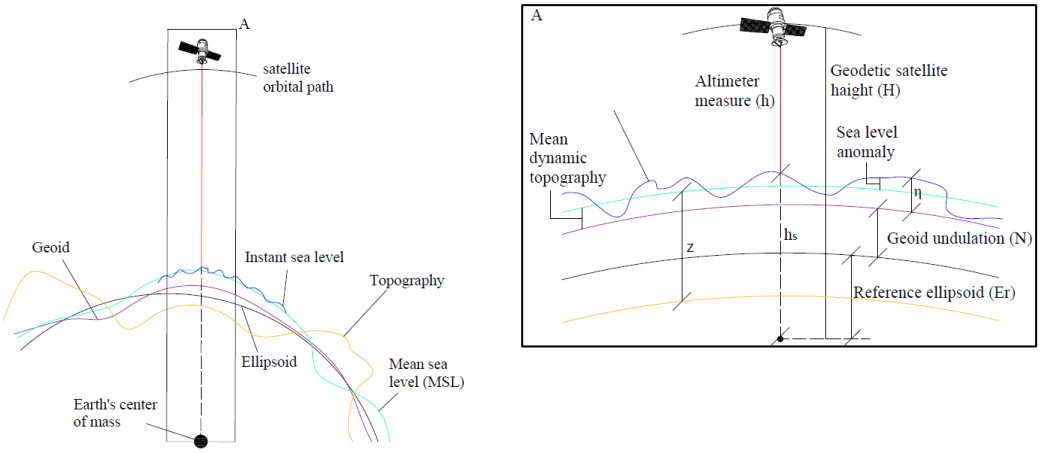

(a) (b)

Figure 10. Schematic representation of the operating principle of a satellite radar altimeter: a) the relationships between the satellite orbit, reference ellipsoid, geoid, mean sea level, and instantaneous sea surface; b) enlarged view detailing the geodetic and oceanographic variables used in the bathymetry extraction process, including satellite height, altimeter range, geoid undulation, sea level anomaly, mean dynamic topography, and depth parameters. Line colors indicate the different surfaces and quantities represented: yellow for topography, blue for the instantaneous sea level, red for the altimeter range measurement, cyan for the mean sea level, and violet for the geoid.

By relating the ToF to the propagation speed of electromagnetic radiation through the atmosphere, the system retrieves the satellite to surface range $h\ (m)$ [162].

The satellite's orbital height $H\ (m)$, defined as the geocentric distance between the satellite and the Earth's center, is determined through a combination of laser ranging, radio-tracking, and GNSS observations, achieving centimetric accuracy [162]. The difference between H and h yields the instantaneous value of the sea surface geocentric height, $h_s\ (m)$, (25):

$$h_s = H - h = SLA + MDT + N + Er \quad (25)$$

- the Sea Level Anomaly (SLA) (m) represents the deviation of the instantaneous sea surface from the mean sea level computed over a reference period. It captures dynamic variability associated with currents, thermal expansion, seasonal and interannual oscillations, and meteorological forcing;
- the Mean Dynamic Topography (MDT) (m) is the long-term mean difference between the mean sea surface and the geoid, reflecting the stationary component of ocean circulation driven by wind stress, density gradients, and other geophysical forcings;
- the geoid undulation, $N\ (m)$, is the vertical separation between the geoid and the reference ellipsoid; when dynamic oceanographic signals such as the MDT and SLA are removed, this surface approximates the long-term mean sea level.
- $Er\ (m)$ is the geocentric distance of the reference ellipsoid.

The averaging of h_s over sufficiently long temporal windows allows the retrieval of the combined contribution of geoid undulations and mean dynamic topography with respect to the ellipsoid [163]. This relationship can be expressed as:

$$SLA = h_s - (MDT + N + Er) \quad (26)$$

that is, the fundamental equation of radar-altimetric bathymetry, which enables large-scale depth estimation through the inversion of sea-surface height anomalies modulated by seafloor topography.

N is related to the distribution of Earth's mass through Bruns' formula (27) and the fundamental equation of physical geodesy (28) [164,165]:

 doi:10.20944/preprints202606.0385.v1

$$N = \frac{T}{\gamma} \tag{27}$$

where T(1/s²) is the gravitational potential, and γ(m/s²) is the normal gravity.

$$\Delta g = -\frac{\partial T}{\partial r} - \frac{2T}{R} \tag{28}$$

where Δg(m/s²) is the gravity anomaly, $\partial T / \partial r$(m/s²) is the radial derivative of T, and R (m) is Earth's radius.

Mass -excess regions relative to the ellipsoid, such as midocean ridges or seamounts, produce positive gravity anomalies that elevate the equipotential surface, whereas mass deficit regions, such as deep basins or abyssal plains, generate negative anomalies, resulting in a local depression of N [164].

These perturbations manifest as changes in the direction of the gravity vector, known as the deflection of the vertical, which corresponds to the slope of the sea surface. This quantity is typically expressed in microradians, with a deflection of 1 μrad corresponds to approximately 1 mm of sea surface height variation per kilometer in plane distance [166].

6.1. Principles of Radar-Altimetric Bathymetry Processing

To infer seafloor topography from gravity anomalies, two main classes of inverse approaches are commonly adopted: the frequency domain and spatial domain approaches [167,168]. Among these, two methodologies are particularly widespread in the literature: the Smith & Sandwell (S&S) frequency domain method and the gravimetric–geological method (GGM), which operates in the spatial domain.

In the S&S method [167,169], gravity anomalies are transformed into the frequency domain using the Fourier transform. For wavelengths between 15 and 200 km, gravity anomalies are linearly related to bathymetry [170] according to Parker's formulation [171] (29).

$$G(k) = Z(k)H_f(k) = 2\pi G_u \Delta\rho \, e^{-2\pi k z^{RA}} H_f(k) \tag{29}$$

Where z^{RA} (m) is the bathymetric depth retrieved by a Radar Altimetric, $G(k)$ (-) is the Fourier transform of the gravity anomaly Δg, $H_f(k)$ (-) is the Fourier transform of seafloor topography, $Z(k)$(-) is the isotropic admittance function, G_u(m³/(kg·s²)) is the gravitational constant, $\Delta\rho$(kg/m³) is the density contrast between rock and seawater.

At longer wavelengths, the gravity–topography relationship becomes nonunique due to lithospheric thickness, whereas at shorter wavelengths the gravity signal is attenuated and noise dominated, limiting bathymetric recovery [166].

The GGM method [26,165,167] separates observed gravity anomalies into short and long wavelength components. Short wavelengths reflect local variations in basement topography, whereas long wavelengths represent deeper mass distributions with gradual spatial variability. The short wavelength component, directly linked to bathymetry, is described by the Bouguer slab approximation [172] (30):

$$\Delta g = 2\pi G_u \Delta\rho \, z^{RA} \tag{30}$$

Recent developments have introduced machine learning based models to enhance bathymetric prediction. For example, Kim et al. (2024) [173] propose an approach aimed at improving the accuracy of GGM derived bathymetry.

6.2. Factors Influencing Measurement Reliability

The accuracy of radar altimetry-derived bathymetry depends on the interaction between instrumental characteristics, orbital configuration, data processing strategies, and environmental conditions. Understanding these factors is essential for assessing data quality and identifying suitable application domains.

 doi:10.20944/preprints202606.0385.v1

A first consideration concerns the depth range that can be reliably inferred, which depends on the relationship between seafloor topography and marine gravity anomalies at wavelengths between 15 and 200 km [170]. Within this spectral band, satellite altimetry provides a fundamental contribution to global seafloor mapping, enabling the reconstruction of major large-scale morphological structures.

Spatial resolution is primarily controlled by the density and distribution of satellite ground tracks. Along track resolution depends on the spacing between consecutive measurements, whereas cross track resolution is strongly influenced by orbital geometry [174]. Typical horizontal resolutions range from 6 to 9 km [175], although values between approximately 1 and 12 km may be achieved under suitable conditions [170].

Accuracy is influenced by multiple factors spanning acquisition and processing stages. These include the instrumental accuracy in measuring the satellite–sea surface range [49], the quality of oceanographic models used to estimate and remove dynamic sea surface signals (e.g., tides, geostrophic currents, waves, seasonal variability) [162], and the performance of gravity field modelling and inversion procedures [49].

Geophysical properties of the subsurface, such as sediment thickness, rock density, and local geological complexity; also affect the gravity–topography relationship. The technique performs best in deep ocean settings, where sediment cover is thin, and seafloor morphology is relatively smooth, such as abyssal plains and continental margins [170]. Typical accuracy values range from 125 to 250 m [176], while under optimal conditions, accuracies on the order of 70 m may be achieved [166].

Within this framework, radar-altimetric bathymetry is inherently suited to the deepest portions of the global ocean, where long-wavelength sea-surface anomalies generated by seafloor topography can be detected and inverted. While its coarse spatial resolution prevents meaningful use in shallow or coastal waters, radar altimetry remains uniquely capable of providing large-scale bathymetric information over abyssal depths of several thousand metres, where no other remote sensing technique is operationally feasible.

7. Emerging and Unconventional Techniques

This section outlines non-conventional and complementary bathymetric techniques that can extend traditional methods in challenging environments. It introduces alternative approaches based on different physical principles, including optical triangulation, thermal sensing, and water-penetrating radar, and summarizes their processing requirements and typical performance (Sections 7.1–7.3). Together, these methods highlight opportunities to improve bathymetric coverage in complex, shallow, or data-poor settings, while remaining limited to specific environmental conditions and not suited for large-scale mapping.

7.1. Principles of Optical Triangulation Derived Bathymetry

Laser light-sheet triangulation operates by projecting a planar or linear laser beam, typically in the green or blue spectral region, onto the target surface [114]. The light reflected or scattered by the illuminated area is recorded by a camera (Figure 11) positioned at a known baseline distance, b, and viewing angle, α, relative to the laser source. Given the fixed geometry between the projector and the camera, the three-dimensional coordinates of the illuminated points can be reconstructed through trigonometric relationships. These coordinates must be corrected for refraction effects, which arise as electromagnetic radiation propagates across media with different refractive indices [115].

Underwater operation is also possible. In this case, the imaging unit is enclosed within pressure resistant housing, while the laser and camera are mounted obliquely relative to the optical window. This configuration ensures that the projected and observed rays intersect at an angle close to orthogonality, thereby maximizing depth sensitivity and minimizing geometric distortions [177].

Owing to their ability to resolve sub-millimetric variations over very short depth ranges (typically <0.5 m), these systems are mainly used in marine biology, plankton studies, and underwater holographic imaging [178]. By accepting a gradual reduction in accuracy, the operational

 doi:10.20944/preprints202606.0385.v1

depth range can be extended to approximately 2.5 m, still outperforming ToF systems, and up to 20 m when using very long baselines (1.24 m), although with reduced precision. These sensors can also be mounted on Remotely Operated Vehicle (ROV) platforms and deployed to depths of up to 4000 m; however, the sensor to target distance remains inherently limited [114].

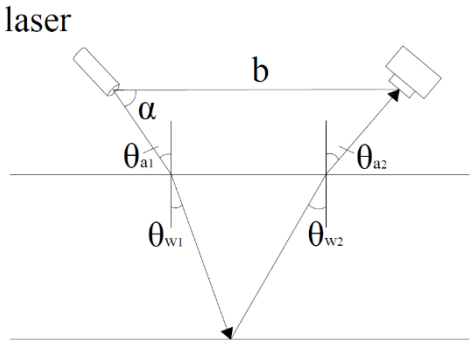

Figure 11. *Schematic representation of optical triangulation.*

7.2. Principles of Thermal Derived Bathymetry

In lacustrine environments characterized by limited hydrodynamics and depths ranging from 10 to 70 m, it has been demonstrated that bathymetry exerts a significant control on the lake's surface thermal response [157,179,180]. This relationship forms the basis for using surface temperature measurements to estimate an *effective depth*, defined as the depth at which a lake thermodynamic model (e.g., FLake) accurately reproduces the observed evolution of surface temperature [181,182]. The physical principle relies on the inversion of equation (31), relating the variations in surface temperature (K/s) to bathymetry through the surface energy balance [181]:

$$\Delta T = \frac{Q_{net}}{\rho_w C_p z^T} \tag{31}$$

Where z^T (m) is the bathymetric depth retrieved by thermal data, Q_{net}(W/m²) is the net surface heat flux, ρ_w(kg/m³) is water density, and C_p(J/(kg·K)) is the specific heat capacity.

The effective depth is estimated as the value of z that minimizes the difference between observed and model simulated surface temperature, thereby ensuring the best representation of the lake's thermal dynamics. A depth of approximately 25 m has been shown to minimize the overall mean error between simulated and observed temperatures [181].

More recent applications have extended the use of thermal data to coastal environments by combining temperature information with spectral reflectance through blackbox machine learning approaches, such as neural networks [183,184]. Although these studies show promising correlations between surface temperature and bathymetry, such approaches currently remain complementary to established techniques, indicating an exploratory research direction that requires further methodological development.

7.3. Principles of Water-Penetrating Radar Bathymetry

WPR enables the extraction of bathymetric information from radargram analysis, which records the intensity and two-way travel time of microwaves reflected from the water surface and the lakebed. Bathymetry is computed as the difference between the WPR–water surface distance and the WPR–lakebed distance, both derived from travel time measurements and corrected for the propagation velocity of electromagnetic waves, which depends on the electromagnetic properties of the media traversed [185,186].

The effectiveness of WPR is strongly influenced by electrical conductivity and dielectric permittivity. Low conductivity and low dielectric permittivity, such as those found in ice; allow

 doi:10.20944/preprints202606.0385.v1

deeper penetration. In freshwater bodies, higher electrical conductivity and the high relative dielectric permittivity of water make bathymetric extraction more challenging. Nevertheless, recent operational applications have successfully employed WPR in shallow lakes (≈2.5 m depth) with conductivities on the order of 200–340 μS/cm, using frequencies typically between 40 and 120 MHz [186]. Due to the strong attenuation of electromagnetic signals, the use of WPR is severely limited in marine and coastal environments; consequently, it remains a niche technique, applicable primarily in shallow freshwater settings [78].

8. Discussion

This section compares the reviewed bathymetric techniques, outlining their strengths, limitations, and applicability across different environments. It evaluates acoustic, optical, LiDAR, radar-altimetric, wave-spectrum, and complementary methods in terms of depth range, operational conditions, and data quality, providing guidance for selecting the most appropriate approach based on survey needs and constraints.

The comparison among the different bathymetric acquisition techniques highlights their respective strengths and limitations, providing essential guidance for selecting the most appropriate methodology. This choice is inherently non-unique and depends strongly on the characteristics of the operational environment as well as on the specific objectives of the survey.

To facilitate this comparison, Table 7 summarizes, for each acquisition technique, the main characteristics of the resulting bathymetric data together with the associated physical and operational factors, whose detailed descriptions have been presented in the preceding sections.

 doi:10.20944/preprints202606.0385.v1

Table 7. Summary of the main characteristics, physical drivers, and operational factors associated with each bathymetric acquisition technique.

Technique	Primary Data Source / Physical Principle	Spatial Resolution	Vertical Accuracy	Environmental Constraints	Operational Constraints	Strengths	Limitations
SBES	Acoustic ToF along a single beam	Low–medium (point-based)	High (cm–dm)	Sensitive to sound speed variability, turbidity, and stratification	Slow coverage; requires a vessel; GNSS/INS integration	Cost-effective; simple operation; reliable depth	Sparse sampling; long survey times; limited in complex morphology
MBES	Acoustic ToF with fan-shaped beam array	High (decimetric–metric)	Very high (cm–dm)	Affected by sound speed profile, sea state, and turbidity	High cost; requires expertise; large data volumes	Full coverage mapping; high detail; robust accuracy	Expensive; complex processing; limited in very shallow water
PDBS	Phase difference measurement across the hydrophone array	Medium–high	Medium	Sensitive to noise, nadir gap, seabed roughness	Moderate cost; high computational load	Wide swath in shallow water; efficient coverage	Lower point accuracy; blind zone at nadir
Radiometric Derived Bathymetry	Light attenuation & spectral response	Medium–high (1–30 m)	Medium (dm–m)	Requires clear water; limited depth (≤20–30 m)	Requires atmospheric correction; sun glint mitigation	Wide coverage; low cost; frequent revisits	Strongly water dependent; lower accuracy than acoustic
Photogrammetry Derived Bathymetry	Multi-view geometry + Snell correction	High (cm–dm)	High in clear water	Requires high water clarity; calm surface	Drone/aircraft deployment; GCPs needed	Very high resolution; ideal for shallow, clear waters	Refraction correction critical; limited depth
LiDAR Bathymetry	Green laser ToF + waveform analysis	High (0.5–5 m)	High (dm)	Requires clear water; depth limit ~50 m	High cost; aircraft required	Rapid coverage; high accuracy; seamless topo bathy	Limited by turbidity; expensive
Radar Altimetry Bathymetry	Radar ToF + gravity topography inversion	Very coarse (100 m–several km)	Low (meters)	Works globally; insensitive to turbidity	Satellite-based; requires geophysical inversion	Global coverage; essential offshore	Not suitable for coastal/shallow waters; coarse resolution

 doi:10.20944/preprints202606.0385.v1

Wave Spectrum Bathymetry	Wave dispersion & celerity inversion	Medium (10–100 m)	Medium (m)	Requires visible wave patterns; limited in calm or stormy seas	Requires SAR/optical/video data; complex inversion	Useful in intermediate depths; large area mapping	Sensitive to wave conditions; indirect method
Thermal-Based Bathymetry	Surface temperature–depth coupling via energy balance	Low–medium	Low–medium	Requires thermally stratified lakes; limited hydrodynamics	Requires thermal time series; model calibration	Useful in lakes; complementary information	Not generalizable; exploratory technique
Water Penetrating Radar Bathymetry	EM wave reflection from the water surface and bed	Very high (cm–dm)	High (dm)	Requires low conductivity; effective only in freshwater	Operates in very shallow waters with low salinity and low electrical conductivity; performance degrades rapidly in turbid, conductive, or wave-disturbed conditions.	Enables non-contact depth estimation in extremely shallow zones	Strongly limited by water conductivity, surface roughness, and bottom reflectivity; applicable only over restricted depth ranges and provides lower accuracy than acoustic or optical methods
Optical Triangulation Derive Bathymetry	Multi-view optical imagery; depth inferred from geometric triangulation and image correspondences	Multi-view optical imagery; depth inferred from geometric triangulation and image correspondences	Moderate; strongly dependent on image matching quality and availability of reference scales	Requires clear, shallow waters; sensitive to turbidity, surface reflections, and illumination variability	Requires stable imaging geometry, accurate camera calibration, and ground control points; limited scalability over large areas	Low-cost data acquisition; suitable for very shallow or complex nearshore environments; effective where radiometric methods fail	Limited depth range (<10–20 m); performance highly dependent on environmental conditions; labor-intensive georeferencing; not suitable for large-scale mapping

 doi:10.20944/preprints202606.0385.v1

A comparative analysis (Table 7) highlights that each bathymetric technique entails a specific trade-off between accuracy, spatial resolution, maximum investigable depth, and the environmental or operational factors that influence measurement reliability.

Satellite radar altimeters enable global coverage of the ocean floor but are limited in spatial resolution and vertical accuracy [115]. Consequently, satellite altimetry is not suitable for applications requiring high precision, such as those related to navigation safety [187]. Altimetric data are more appropriate for regional to global scale analyses. A notable example is their use in generating baseline bathymetric grids subsequently refined with higher accuracy datasets, as in the GEBCO_2014 global bathymetric model [188].

Acoustic bathymetric techniques currently represent the most established approach for seafloor mapping, owing to their high accuracy and operational robustness, and they constitute the reference standard for numerous applications [189]. These systems provide reliable measurements across a wide depth range and are applicable in both shallow and deep waters, including highly turbid environments where optical techniques are severely constrained [190]. However, the use of acoustic systems also presents several challenges, motivating the development and adoption of alternative or complementary techniques [138]. Acoustic measurements are sensitive to variations in the physical properties of the medium, such as temperature and salinity, as well as to sea state conditions and platform dynamics [95]. From an operational and economic perspective, acoustic surveys require high-cost instrumentation, vessel deployment, specialized personnel, and long acquisition times. Even when using unmanned platforms such as ROVs or autonomous systems, a support vessel is typically required, further increasing operational costs [35]. In shallow waters (<50 m), the reduced swath width of acoustic systems significantly increases acquisition time and labor requirements, affecting overall efficiency [138]. Additionally, growing environmental concerns regarding the use of sound in marine ecosystems, given that many fish species and marine mammals rely on acoustic cues for navigation and communication, have raised issues related to the potential ecological impact of sonar, making authorization procedures more complex in some countries (“Habitat Directive – Environment – European Commission,” 2026) [191].

Active optical techniques represent one of the most established methods for mapping shallow waters, offering good accuracy, wide spatial coverage, and high operational efficiency. These techniques are particularly suitable for surveying coastal areas that are difficult to access using traditional methods, such as rugged coastlines, complex rocky environments, or coral reefs, while also ensuring seamless coverage across the land–sea interface [70]. As active systems, they can operate independently of solar illumination, providing high operational flexibility. However, the limited penetration of electromagnetic radiation in water restricts their applicability to clear and shallow water environments. In highly turbid waters or at greater depths, measurement accuracy decreases markedly. Moreover, compared with multibeam sonar, bathymetric LiDAR generally provides lower spatial resolution. Finally, the high operational costs associated with airborne platforms and specialized instrumentation may limit large-scale deployment [192].

Passive optical techniques based on radiometric approaches are particularly effective in shallow, clear-water coastal environments. However, bathymetric accuracy degrades rapidly with increasing depth, primarily due to the attenuation of electromagnetic radiation within the water column, as discussed in Section 4.3 [135]. These methods also perform poorly in turbid waters and in the presence of submerged vegetation, which significantly alters the spectral response of the seabed [78]. Overall, the achievable accuracy is lower than that of active techniques such as bathymetric LiDAR and multibeam sonar [187]. Nevertheless, their low operational cost supports their use in a variety of applications.

An alternative passive approach is optical photogrammetry, which is particularly suitable for very shallow waters (<20 m), where radiometric methods often become ineffective due to environmental heterogeneity, uncertain atmospheric corrections, or the absence of in situ depth measurements [71,75]. Additional advantages include relatively low costs [135]. However, metric reconstruction of bathymetry using photogrammetry requires known reference scales (e.g., a

 doi:10.20944/preprints202606.0385.v1

reference length), obtained through stereo system calibration or through seabed control points acquired using traditional surveying techniques or sonar systems [193]. Georeferencing and validation procedures are often time and resource demanding and are difficult to scale over large areas, limiting the applicability of this technique primarily to spatially restricted environments [194].

Wave spectrum based bathymetric techniques represent an alternative approach for reconstructing coastal bathymetry. These methods are particularly advantageous in contexts where optical techniques face significant limitations. Unlike optical bathymetry, WSB methods do not depend on water clarity or seabed reflectance, making them suitable for turbid environments or areas with variable optical properties [27]. A further advantage is the ability to acquire data using SAR sensors under cloud cover, at night, and in most weather conditions, except during intense precipitation, unlike optical sensors, which are strongly affected by cloud cover and solar illumination [195]. WSB methods are also effective in detecting largescale geomorphological features and in highly dynamic environments, such as sandbanks and shoals, where bathymetry undergoes frequent and rapid changes [187]. However, their applicability and accuracy are strongly influenced by sea-state conditions, particularly wind direction and intensity, as well as by acquisition geometry [157]. Under low significant wave heights, wavefield visibility may be limited, compromising bathymetric estimation reliability [160]. Furthermore, WSB derived products generally exhibit lower spatial resolution and accuracy than those obtained with acoustic and optical techniques, limiting their use in high-precision operational applications such as navigation risk assessment [187].

In addition to the main methodological families, emerging and unconventional techniques offer complementary solutions in environments where traditional acoustic, optical, or altimetric approaches face significant limitations. Optical-triangulation-derived bathymetry provides a geometric alternative for very shallow waters or complex nearshore settings, although its applicability is constrained by illumination conditions and the need for well-defined image correspondences. Thermal-derived bathymetry exploits temperature-related surface patterns to infer depth indirectly, making it suitable for specific hydrodynamic contexts but inherently limited by the transient nature of thermal contrasts. Water-penetrating radar techniques represent a promising frontier for mapping extremely shallow or turbid waters, although their performance remains strongly dependent on substrate properties and electromagnetic penetration capabilities. While these methods generally offer lower accuracy than established acoustic or active optical systems, they expand the range of feasible survey conditions and can provide valuable supplementary information in data-poor or operationally challenging environments.

A comparison of the depth domains accessible to the different bathymetric methodologies (Figure 12) highlights how the operational ranges of each technique are intrinsically constrained by the physical principles on which they are based. The logarithmic depth scale accentuates the pronounced variability in applicability, revealing a clear transition from shallow-water approaches, such as optical, radiometric, thermal, and LiDAR methods, to deeper-water solutions, including acoustic systems, wave-spectrum inversion, and radar-altimetric bathymetry. These ranges should be regarded as indicative rather than absolute, since the effective penetration depth is influenced by multiple factors, including the specific implementation of processing algorithms within each methodological category. Overall, the depth-dependent variability observed reinforces the need for a context-driven selection of bathymetric techniques and supports the broader conclusion that no single method can adequately address the full spectrum of marine environments.

 doi:10.20944/preprints202606.0385.v1

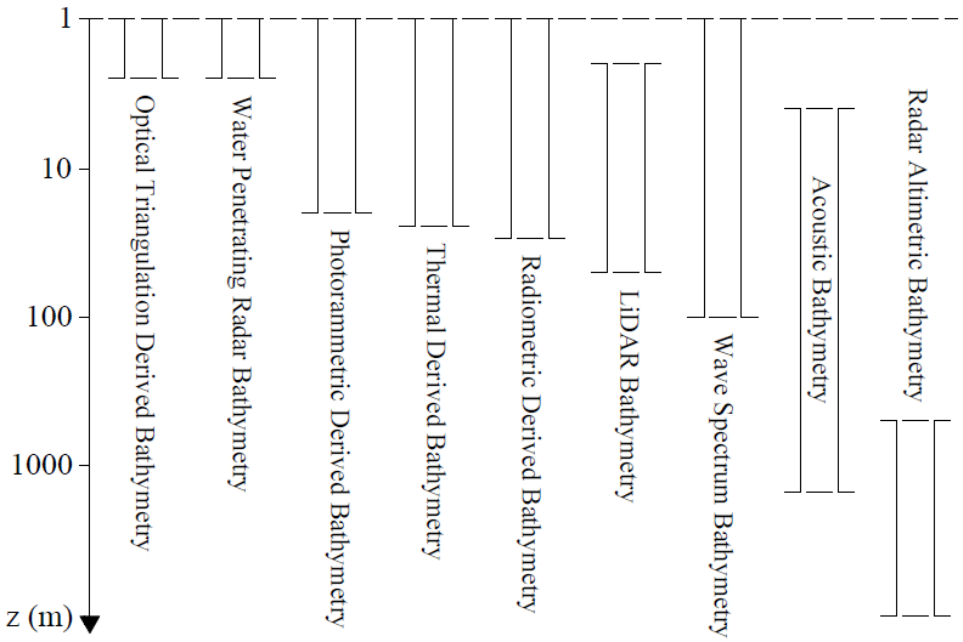

Figure 12. *Operational depth ranges of common bathymetric techniques, displayed on a logarithmic depth scale. The shoreline depth (0 m) is not represented due to the logarithmic axis; consequently, the 1 m depth is shown with a dashed line. The reported ranges are indicative rather than strict, as they depend on several factors, including local water properties and the specific implementation of the algorithms within each methodological category.*

Selecting the most appropriate bathymetric technique, therefore, requires a careful balance between accuracy, spatial resolution, cost, and operational conditions. In this context, integrated and multi-sensor approaches are becoming increasingly established. Their primary objective is to fuse observations from heterogeneous sources to enhance the accuracy, completeness, and spatial continuity of the final bathymetric model, as well as to improve operational robustness [36,64]. However, during data processing, it is essential to compensate for typical multi-source discrepancies, such as temporal acquisition differences, spatial misalignments, and heterogeneous coverage.

A notable example of an integrated approach is the combination of satellite optical imagery with echo-sounder measurements. In this context, in situ data are used to calibrate satellite-based depth-retrieval algorithms, enabling the wide spatial coverage of satellite imagery to be combined with the high reliability of acoustic point measurements [94]. Another example is the integration of bathymetric LiDAR with multibeam echo sounders, which improves overall survey accuracy and ensures continuous coverage from shallow to deeper waters [196]. Finally, at broader spatial scales, the integration of satellite altimetry with multibeam bathymetry has proven particularly effective in improving depth estimation in poorly surveyed areas, contributing to a more coherent and reliable representation of seafloor morphology [26,188].

9. Conclusions

The present review has examined the main sensors and techniques used for bathymetric data acquisition and extraction, the underlying physical principles, and the processing workflows that influence achievable depth ranges, spatial resolution, and accuracy. The primary objective was to provide a comparative framework to support the selection of the most appropriate technique based on objective criteria such as sensor specifications, environmental characteristics, accuracy requirements, spatial resolution, and intended application, ultimately contributing to overcoming current knowledge gaps.

This review has examined the main bathymetric acquisition techniques based on acoustic, optical, and radar sensing, highlighting their respective principles, capabilities, and limitations.

 doi:10.20944/preprints202606.0385.v1

Satellite radar altimetry enables global seafloor coverage through the relationship between sea surface height and gravity-driven seafloor features, although with relatively low spatial resolution and vertical accuracy.

Acoustic methods, based on sound wave travel time and supported by ancillary data and processing steps, remain the most accurate and robust solution for seafloor mapping, despite high operational costs, particularly in shallow environments.

Optical techniques provide effective alternatives in shallow waters. Active systems such as bathymetric LiDAR offer a balance between accuracy, coverage, and efficiency, while passive radiometric and photogrammetric approaches represent cost-effective solutions, though generally with lower accuracy and greater sensitivity to environmental conditions.

Wave Spectrum Bathymetry emerges as a complementary approach, enabling depth estimation from surface wave characteristics and offering advantages in turbid waters, albeit with lower resolution and accuracy compared to acoustic and optical methods.

Finally, non-conventional techniques, including thermal and ground-penetrating radar approaches, may support bathymetric retrieval in specific environments but remain limited in scope and not suitable for large-scale applications.

Overall, the analysis highlights that no single technique is universally optimal, and that the selection of the most appropriate method depends on depth range, environmental conditions, operational constraints, and required data quality.

An outcome of this review is that each technique exhibits a characteristic depth range of applicability: acoustic systems remain the only solution capable of providing reliable measurements from very shallow waters to abyssal depths, with multibeam sonars ensuring high-resolution mapping across the full depth spectrum; passive and active optical methods are restricted to shallow, optically clear environments, typically from the shoreline to a few tens of metres, where water clarity allows sufficient light penetration; airborne or satellite LiDAR bathymetry extends this range further, but remains fundamentally limited by water turbidity and attenuation; radar-altimetric approaches operate at the opposite end of the spectrum, enabling coarse-resolution bathymetric inference over deep-ocean basins where no other remote technique is feasible; and wave-spectrum methods apply only in shallow, wave-dominated coastal zones, where wave transformation is strongly controlled by seafloor morphology.

Despite the wide range of techniques analyzed, this review highlights several limitations in both the literature and available data. Accuracy metrics are often inconsistent, reported in different ways, and difficult to compare due to variations in data acquisition, environmental conditions, spatial scales, and processing methods. This variability makes it challenging to evaluate accuracy objectively, applicability range, and to establish standardized benchmarks for comparing bathymetric approaches.

Overall, this review highlights that the most effective bathymetric solutions do not rely on a single technology, but rather on integrated multisensor approaches capable of overcoming the limitations of individual techniques and improving the accuracy, completeness, and spatial continuity of the resulting bathymetric models.

Future developments are expected to increasingly focus on the integration of multi-source data, supported by emerging technologies such as unmanned surface vehicles, miniaturized sensors, and advances in satellite LiDAR bathymetry, which together have the potential to further enhance the efficiency and scalability of bathymetric reconstruction.

These approaches have the potential to reduce operational costs, increase acquisition flexibility, and improve spatial coverage, thereby contributing to closing the current knowledge gap and making bathymetric mapping more efficient and accessible.

Supplementary Materials: The following supporting information can be downloaded at the website of this paper posted on Preprints.org.

 doi:10.20944/preprints202606.0385.v1

Author Contributions: All authors contributed to this study and have read and agreed to the published version of the manuscript. Writing original draft, review – NAS, AM; Writing– NAS, MLB, GC, AM.

Funding: This research is supported under the National Recovery and Resilience Plan (NRRP), Mission 4 Component 2 Investment 1.4 – Call for tender No. 3138 of 16 December 2021, rectified by Decree n.3175 of 18 December 2021 of Italian Ministry of University and Research funded by the European Union – under the NextGenerationEU initiative. Project code CN_00000033, Concession Decree No. 1034 of 17 June 2022 adopted by the Italian Ministry of University and Research, CUP: B73C22000790001, Project title "National Biodiversity Future Center – NBFC, and by Planetek Italia S.r.l.

Conflicts of Interest: The authors declare no conflicts of interest.

Abbreviations

The following abbreviations are used in this manuscript:

Acronym	Expansion
ALB	Airborne LiDAR Bathymetry
ANNs	Artificial Neural Networks
CDOM	colored dissolved organic matter
DCDB	Data Centre for Digital Bathymetry
FWF	full-waveform
GCPs	Ground Control Points
GEBCO	General Bathymetric Chart of the Oceans
GGM	gravimetric–geological method
GNSS	Global Navigation Satellite System
IHO	International Hydrographic Organization
IMU	inertial measurement unit
MBES	multibeam echo sounders
PC1	first principal component
PCA	Principal Component Analysis
PDBS	Phase-Differencing Bathymetric Sonar
ROV	Remotely Operated Vehicle
S&S	Smith & Sandwell method
SAR	synthetic aperture radar
SBES	single-beam echo sounders
SfM	Structure-from-Motion
SOM	Self-Organizing Maps
SSS	Side-scan sonar
TOA	Time of Arrival
ToF	time-of-flight
WPR	Water-Penetrating Radar
WSB	Wave Spectrum Bathymetric

Symbol	Variable	Units
C	wave celerity	(m/s)
C_p	specific heat capacity	(J/(kg·K)
c	speed of light in air	(m/s)
d	draft	(m)
Er	geocentric distance of the reference ellipsoid	(m)
f	wave frequency	(1/s)
G(k)	Fourier transform of the gravity anomaly Δg	(-)
G_u	gravitational constant	(m^3/(kg·s^2))
g	gravitational acceleration	(m/s^2)
H	satellite's orbital height	(m)
H_f(k)	Fourier transform of seafloor topography	(-)
h	satellite-to-surface range	(m)
h_0	empirical coefficient	(m)

 doi:10.20944/preprints202606.0385.v1

h_i	empirical coefficient	(m)
h_s	instantaneous value of the sea surface geocentric height	(m)
k	wavenumber	(1/m)
$k_d(\lambda)$	diffuse attenuation coefficient	(1/m)
kx	wavenumber in the x direction	(1/m)
ky	wavenumber in the y direction	(1/m)
L	wavelength	(m)
l	empirical constant	(-)
MDT	Mean Dynamic Topography	(m)
m_0	offset corresponding to z = 0 m	(m)
m_1	scaling constant	(-)
m_{kd}	quadratic attenuation coefficient	($1/m^2$)
N	geoid undulation	(m)
n	refractive index	(-)
n_w	refractive index of water	(-)
p	empirically derived correction factor	(-)
p_{FMVi}	probability associated with the point, obtained by Fuzzy Majority Voting	(-)
Q_{net}	net surface heat flux	(W/m^2)
q_{kd}	linear attenuation coefficient	(1/m)
R	Earth's radius	(m)
$<R^{0-}(\lambda)>$	reflectance just below the surface, averaged over the spectrum and time	(-)
$R^{0-}(\lambda)$	reflectance just-below-surface	(-)
$R_\infty(\lambda)$	infinitely deep-water reflectance	(-)
R_b	reflectances in the blue band	(-)
$R_B(\lambda)$	bottom reflectance	(-)
$R_C(\lambda)$	water-column reflectance	(-)
R_g	reflectances in the green band	(-)
R_i	reflectance in band *i*, corrected for atmospheric effects and sun-glint	(-)
$R_P(\lambda)$	atmospheric direct and diffuse reflectance	(-)
$R_S(\lambda)$	surface-reflected component	(-)
$R_T(\lambda)$	total reflectance recorded by the sensor	(-)
SLA	Sea Level Anomaly	(m)
T	gravitational potential	($1/s^2$)
T_b	total two-way travel time of the bottom return	(s)
T_s	two-way travel time of the surface return	(s)
T_w	two-way travel time in water	(s)
t	way travel time	(s)
v	sound speed	(m/s)
Z(k)	isotropic admittance function	(-)
z	water depth	(m)
$\bar{z}$	mean depth	(m)
z_a	apparent depth	(m)
z^{EES}	bathymetric depth retrieved by an echo sounder system	(m)
z_i	depth of training points	(m)
z^{Li}	bathymetric depth retrieved by LiDAR data	(m)
z^{P}	bathymetric depth retrieved by photogrammetric data	(m)
z^{PDBS}	bathymetric depth retrieved by a PDBS	(m)
z^{R}	bathymetric depth retrieved by radiometric data	(m)
z^{RA}	bathymetric depth retrieved by a Radar Altimetric	(m)
z^{R}_{ANNs}	estimated depth	(m)
z^{T}	bathymetric depth retrieved by thermal data	(m)
z^{WBS}	bathymetric depth retrieved by WSB	(m)
z_{ws}	water-surface elevation	(m)
ϭ	offset term	(-)
γ	normal gravity	(m/s^2)
Δg	the gravity anomaly	(m/s^2)
ΔT	variations in surface temperature	(K/s)
Δϱ	density contrast between rock and seawater	(kg/m^3)
∂T/∂r	radial derivative of T	(m/s^2)

 doi:10.20944/preprints202606.0385.v1

θ	angle of arrival of the reflected signal	(rad)
θ_{a1}	incidence angles between the incoming rays and the surface normal in air at left	(rad)
θ_{a2}	incidence angles between the incoming rays and the surface normal in air at right	(rad)
θ_{dir}	dominant wave direction	(rad)
θ_w	refraction angles in water	(rad)
θ_{w1}	refraction angles in water at left	(rad)
θ_{w2}	refraction angles in water at right	(rad)
ϱ_w	water density	(kg/m^3)

References

1. Agrafiotis, P.; Skarlatos, D.; Georgopoulos, A.; Karantzalos, K. DepthLearn: Learning to Correct the Refraction on Point Clouds Derived from Aerial Imagery for Accurate Dense Shallow Water Bathymetry Based on SVMs-Fusion with LiDAR Point Clouds. *Remote Sensing* **2019**, *11*, 2225, doi:10.3390/rs11192225.
2. Abualtayef, M.; Rabou, M.A.; Afifi, S.; Rabou, A.F.A.; Seif, A.K.; Masria, A. Change Detection of Gaza Coastal Zone Using GIS and Remote Sensing Techniques. *J Coast Conserv* **2021**, *25*, 36, doi:10.1007/s11852-021-00825-4.
3. Rzhanov, Y.; Cutter, G.R.; Mayer, L.A. Seafloor Segmentation Based on Bathymetric Measurements from Multibeam Echosounder Data. In Proceedings of the Seventh International Symposium on Signal Processing and Its Applications, 2003. Proceedings.; July 2003; Vol. 1, pp. 529–532 vol.1.
4. Wölfl, A.-C.; Snaith, H.; Amirebrahimi, S.; Devey, C.W.; Dorschel, B.; Ferrini, V.; Huvenne, V.A.I.; Jakobsson, M.; Jencks, J.; Johnston, G.; et al. Seafloor Mapping – The Challenge of a Truly Global Ocean Bathymetry. *Front. Mar. Sci.* **2019**, *6*, doi:10.3389/fmars.2019.00283.
5. Gabr, B.; Ahmed, M.; Marmoush, Y. PlanetScope and Landsat 8 Imageries for Bathymetry Mapping. *Journal of Marine Science and Engineering* **2020**, *8*, 143, doi:10.3390/jmse8020143.
6. Hell, B.; Broman, B.; Jakobsson, L.; Jakobsson, M.; Magnusson, Å.; Wiberg, P. The Use of Bathymetric Data in Society and Science: A Review from the Baltic Sea. *Ambio* **2012**, *41*, 138–150, doi:10.1007/s13280-011-0192-y.
7. Samaras, A.G.; Gaeta, M.G.; Miquel, A.M.; Archetti, R. High-Resolution Wave and Hydrodynamics Modelling in Coastal Areas: Operational Applications for Coastal Planning, Decision Support and Assessment. *Natural Hazards and Earth System Sciences* **2016**, *16*, 1499–1518, doi:10.5194/nhess-16-1499-2016.
8. Peters, M.D.J.; Marnie, C.; Tricco, A.C.; Pollock, D.; Munn, Z.; Alexander, L.; McInerney, P.; Godfrey, C.M.; Khalil, H. Updated Methodological Guidance for the Conduct of Scoping Reviews. *JBI Evidence Synthesis* **2020**, *18*, 2119, doi:10.11124/JBIES-20-00167.
9. Gizachew, B. Artificial Intelligence and Machine Learning in Remote Sensing for Tropical Forest Monitoring: Applications, Challenges, and Emerging Solutions. *Remote Sensing* **2026**, *18*, 1193, doi:10.3390/rs18081193.
10. Communicatie, F.M.& Home | IHO Available online: https://iho.int/ (accessed on 25 March 2026).
11. International Hydrographic Organization (IHO) IHO Data Centre for Digital Bathymetry (DCDB) | National Centers for Environmental Information (NCEI) Available online: https://www.ncei.noaa.gov/iho-data-centre-digital-bathymetry (accessed on 25 March 2026).
12. GEBCO Compilation Group GEBCO | General Bathymetric Chart of the Oceans Available online: https://www.gebco.net/ (accessed on 25 March 2026).
13. GEBCO Compilation Group Gridded Bathymetry Data | GEBCO Available online: https://www.gebco.net/data-products/gridded-bathymetry-data (accessed on 25 March 2026).
14. GEBCO Compilation Group GEBCO Multi-Resolution Grid Product | GEBCO Available online: https://www.gebco.net/data-products/gridded-bathymetry-data/multi-res (accessed on 25 March 2026).
15. Nippon Foundation–GEBCO Seabed 2030 Project Home — Seabed 2030 Available online: https://seabed2030.org/ (accessed on 25 March 2026).
16. EMODnet Bathymetry Consortium EMODnet Digital Bathymetry (DTM 2024) 2024.
17. Australia, c\=AU\;o\=Australia G. Data Portal Available online: https://www.ausseabed.gov.au/data (accessed on 25 March 2026).

 doi:10.20944/preprints202606.0385.v1

18. JAMSTEC JAMSTEC Contribution to The Nippon Foundation – GEBCO Seabed 2030 Project Available online: https://www.jamstec.go.jp/seabed2030/e/ (accessed on 25 March 2026).
19. NOAA National Centers for Environmental Information Bathymetric Data Viewer Available online: https://www.ncei.noaa.gov/maps/bathymetry/ (accessed on 25 March 2026).
20. IBCSO (International Bathymetric Chart of the Southern Ocean) IBCSO Current Release | IBCSO Available online: https://ibcso.org/current_version/ (accessed on 25 March 2026).
21. IBCAO Compilation Group International Bathymetric Chart of the Arctic Ocean (IBCAO) | GEBCO Available online: https://www.gebco.net/data-products/gridded-bathymetry-data/arctic-ocean (accessed on 25 March 2026).
22. Thierry, S.; Dick, S.; George, S.; Benoit, L.; Cyrille, P. EMODnet Bathymetry a Compilation of Bathymetric Data in the European Waters. In Proceedings of the OCEANS 2019 - Marseille; June 2019; pp. 1–7.
23. MAREANO Programme Bathymetric Data Available online: https://www.mareano.no/en/maps-and-data/marine-geospatial-data (accessed on 25 March 2026).
24. Istituto Idrografico della Marina Istituto Idrografico della Marina Available online: https://www.istitutoidrografico.it/it/index.html (accessed on 25 March 2026).
25. Federal Maritime and Hydrographic Agency (BSH) BSH - Hydrographic Surveying Available online: https://www.bsh.de/EN/DATA/Marine-use/Hydrographic_surveying/hydrographic_surveying_node.html (accessed on 25 March 2026).
26. Chen, X.; Yang, M.; Sun, M.; Li, W.; An, D.; Feng, P.; Feng, W.; Zhong, M. Enhancing Bathymetry Estimation from Altimeter-Derived Gravity in Shallow to Intermediate Seas by Integrating Coastline and SDB Constraints. *Advances in Space Research* **2025**, *76*, 4959–4976, doi:10.1016/j.asr.2025.07.094.
27. Leu, L.-G.; Chang, H.-W. Remotely Sensing in Detecting the Water Depths and Bed Load of Shallow Waters and Their Changes. *Ocean Engineering* **2005**, *32*, 1174–1198, doi:10.1016/j.oceaneng.2004.12.005.
28. Roberts, A.M.; Kusznir, N.J.; Yielding, G.; Beeley, H. Mapping the Bathymetric Evolution of the Northern North Sea: From Jurassic Synrift Archipelago through Cretaceous–Tertiary Post-Rift Subsidence. *Petroleum Geoscience* **2019**, *25*, 306–321, doi:10.1144/petgeo2018-066.
29. Hoffmann, T.; Pfennings, K.; Hitzegrad, J.; Paul, M.; Wehrmann, A.; Goseberg, N.; Schlurmann, T. Sediment Accumulation by Coastal Biogenic Structures Sustains Intertidal Flats Facing Sea Level Rise in the German Wadden Sea. *Scientific Reports* **2025**, *15*, doi:10.1038/s41598-025-03326-8.
30. Bale, A.; Uncles, R.; Villena-Lincoln, A.; Widdows, J. An Assessment of the Potential Impact of Dredging Activity on the Tamar Estuary over the Last Century: Bathymetric and Hydrodynamic Changes. *Hydrobiologia* **2007**, *588*, 83–95, doi:10.1007/s10750-007-0654-1.
31. Moretto, J.; Rigon, E.; Mao, L.; Delai, F.; Picco, L.; Lenzi, M.A. Short-Term Geomorphic Analysis in a Disturbed Fluvial Environment by Fusion of LiDAR, Colour Bathymetry and dGPS Surveys. *CATENA* **2014**, *122*, 180–195, doi:10.1016/j.catena.2014.06.023.
32. Dierssen, H.; Theberge, A. Bathymetry: History of Seafloor Mapping. In; 2014; pp. 1–6 ISBN 978-1-4398-5258-3.
33. Santos, D.; Abreu, T.; Silva, P.A.; Baptista, P. Estimation of Coastal Bathymetry Using Wavelets. *Journal of Marine Science and Engineering* **2020**, *8*, 772, doi:10.3390/jmse8100772.
34. Guo, K.; Li, Q.; Wang, C.; Mao, Q.; Liu, Y.; Zhu, J.; Wu, A. Development of a Single-Wavelength Airborne Bathymetric LiDAR: System Design and Data Processing. *ISPRS Journal of Photogrammetry and Remote Sensing* **2022**, *185*, 62–84, doi:10.1016/j.isprsjprs.2022.01.011.
35. Ferreira, I.O.; Andrade, L.C. de; Teixeira, V.G.; Santos, F.C.M. State of Art of Bathymetric Surveys. *Bol. Ciênc. Geod.* **2022**, *28*, e2022002, doi:https://doi.org/10.1590/s1982-21702022000100002.
36. Giordano, F.; Mattei, G.; Parente, C.; Peluso, F.; Santamaria, R. Integrating Sensors into a Marine Drone for Bathymetric 3D Surveys in Shallow Waters. *Sensors* **2016**, *16*, 41, doi:10.3390/s16010041.
37. Zhao, L.; Bai, Y.; Paik, J.K. Optimal Coverage Path Planning for USV-Assisted Coastal Bathymetric Survey: Models, Solutions, and Lake Trials. *Ocean Engineering* **2024**, *296*, 116921, doi:10.1016/j.oceaneng.2024.116921.
38. Lamarche, G.; Lurton, X. Recommendations for Improved and Coherent Acquisition and Processing of Backscatter Data from Seafloor-Mapping Sonars. *Mar Geophys Res* **2018**, *39*, 5–22, doi:10.1007/s11001-017-9315-6.

 doi:10.20944/preprints202606.0385.v1

39. Im, S.-U.; Lee, C.-A.; Lim, M.; Kim, C.; Paeng, D.-G. Sound Absorption of the Water Column and Its Calibration for Multibeam Echosounder Backscattered Mapping in the East Sea of Korea. *Applied Sciences* **2025**, *15*, doi:10.3390/app15031131.
40. Constantinoiu, L.-F.; Bernardino, M.; Rusu, E. Autonomous Shallow Water Hydrographic Survey Using a Proto-Type USV. *Journal of Marine Science and Engineering* **2023**, *11*, 799, doi:10.3390/jmse11040799.
41. Zhang, W.; Jin, S.; Bian, G.; Peng, C.; Xia, H. A Method for Full-Depth Sound Speed Profile Reconstruction Based on Average Sound Speed Extrapolation. *Journal of Marine Science and Engineering* **2024**, *12*, 930, doi:10.3390/jmse12060930.
42. Amoroso, P.P.; Parente, C. The Importance of Sound Velocity Determination for Bathymetric Survey. *Acta IMEKO* **2021**, *10*, 46–53, doi:10.21014/acta_imeko.v10i4.1120.
43. Ismail, N.; Md Din, A.H.; Hamden, M.; Zulkifli, N.A.; M Idris, K. REDUCTION OF MEAN SEA LEVEL DEPTH BASED ON TIDE GAUGE DISTANCE-DEPENDENT AT SUNGAI DINDING, LUMUT. *The International Archives of the Photogrammetry, Remote Sensing and Spatial Information Sciences* **2023**, *XLVIII-4/W6-2022*, 167–177, doi:10.5194/isprs-archives-XLVIII-4-W6-2022-167-2023.
44. Bio, A.; Gonçalves, J.A.; Magalhães, A.; Pinheiro, J.; Bastos, L. Combining Low-Cost Sonar and High-Precision Global Navigation Satellite System for Shallow Water Bathymetry. *Estuaries and Coasts* **2022**, *45*, 1000–1011, doi:10.1007/s12237-020-00703-6.
45. Stateczny, A.; Specht, C.; Specht, M.; Brčić, D.; Jugović, A.; Widźgowski, S.; Wiśniewska, M.; Lewicka, O. Study on the Positioning Accuracy of GNSS/INS Systems Supported by DGPS and RTK Receivers for Hydrographic Surveys. *Energies* **2021**, *14*, 7413, doi:10.3390/en14217413.
46. Barkby, S.; Williams, S.; Pizarro, O.; Jakuba, M. An Efficient Approach to Bathymetric SLAM. In Proceedings of the 2009 IEEE/RSJ International Conference on Intelligent Robots and Systems; October 2009; pp. 219–224.
47. Calder, B.R.; Mayer, L.A. Automatic Processing of High-Rate, High-Density Multibeam Echosounder Data. *Geochemistry, Geophysics, Geosystems* **2003**, *4*, doi:10.1029/2002GC000486.
48. Ferreira, I.O.; Santos, A. de P. dos; Oliveira, J.C. de; Medeiros, N. das G.; Emiliano, P.C. ROBUST METHODOLOGY FOR DETECTION OF SPIKES IN MULTIBEAM ECHO SOUNDER DATA. *Bol. Ciênc. Geod.* **2019**, *25*, e2019014, doi:https://doi.org/10.1590/s1982-21702019000300014.
49. Li, Z.; Peng, Z.; Zhang, Z.; Chu, Y.; Xu, C.; Yao, S.; García-Fernández, Á.F.; Zhu, X.; Yue, Y.; Levers, A.; et al. Exploring Modern Bathymetry: A Comprehensive Review of Data Acquisition Devices, Model Accuracy, and Interpolation Techniques for Enhanced Underwater Mapping. *Front. Mar. Sci.* **2023**, *10*, doi:10.3389/fmars.2023.1178845.
50. Brisson, L.N.; Wolfe, D.A. Interferometric Swath Bathymetry for Large Scale Shallow Water Hydrographic Surveys. **2014**.
51. Grall, P.; Kochanska, I.; Marszal, J. Direction-of-Arrival Estimation Methods in Interferometric Echo Sounding. *Sensors* **2020**, *20*, 3556, doi:10.3390/s20123556.
52. Coiras, E.; Petillot, Y.; Lane, D.M. Multiresolution 3-D Reconstruction From Side-Scan Sonar Images. *IEEE Transactions on Image Processing* **2007**, *16*, 382–390, doi:10.1109/TIP.2006.888337.
53. Wu, Z.; Yang, F.; Tang, Y. Side-Scan Sonar and Sub-Bottom Profiler Surveying | Springer Nature Link Available online: https://link.springer.com/chapter/10.1007/978-981-15-9750-3_4 (accessed on 3 March 2026).
54. Saleh, M.; Rabah, M. Seabed Sub-Bottom Sediment Classification Using Parametric Sub-Bottom Profiler. *NRIAG Journal of Astronomy and Geophysics* **2016**, *5*, 87–95, doi:10.1016/j.nrjag.2016.01.004.
55. Zheng, Z.; Jiang, S.; Zeng, W. Comparing Measurement Correction of Echo Sounder in Shallow-Water Area. *Acta Geophys.* **2022**, *70*, 1677–1686, doi:10.1007/s11600-022-00802-x.
56. Bannari, A.; Kadhem, G. MBES-CARIS Data Validation for Bathymetric Mapping of Shallow Water in the Kingdom of Bahrain on the Arabian Gulf. *Remote Sensing* **2017**, *9*, 385, doi:10.3390/rs9040385.
57. Nadzir, Z.A.; Munthe, M.B.U. UTILIZATION OF MULTIBEAM ECHOSOUNDER DATA FOR BATHYMETRY MAPPING: EVALUATION WITH INTERNATIONAL STANDARD. *JGE (Jurnal Geofisika Eksplorasi)* **2025**, *11*, 5–15, doi:10.23960/jge.v11i1.483.

 doi:10.20944/preprints202606.0385.v1

58. Mujta, W.; Wlodarczyk-Sielicka, M.; Stateczny, A. Testing the Effect of Bathymetric Data Reduction on the Shape of the Digital Bottom Model. *Sensors* **2023**, *23*, 5445, doi:10.3390/s23125445.
59. Calder, B.R.; Mayer, L.A. Automatic Processing of High-Rate, High-Density Multibeam Echosounder Data. *Geochemistry, Geophysics, Geosystems* **2003**, *4*, doi:10.1029/2002GC000486.
60. Wlodarczyk-Sielicka, M.; Stateczny, A. Comparison of Selected Reduction Methods of Bathymetric Data Obtained by Multibeam Echosounder. In Proceedings of the 2016 Baltic Geodetic Congress (BGC Geomatics); IEEE: Gdansk, Poland, June 2016; pp. 73–77.
61. Wlodarczyk-Sielicka, M.; Stateczny, A. Clustering Bathymetric Data for Electronic Navigational Charts. *Journal of Navigation* **2016**, *1*, 1–11, doi:10.1017/S0373463316000035.
62. Błaszczak-Bąk, W.; Sobieraj-Żłobińska, A.; Kowalik, M. The OptD-Multi Method in LiDAR Processing. *Meas. Sci. Technol.* **2017**, *28*, 075009, doi:10.1088/1361-6501/aa7444.
63. Stateczny, A.; Wlodarczyk-Sielicka, M. (PDF) Reti Neurali Artificiali Auto-Organizzate Nel Processo Di Riduzione Dei Big Data Idrografici Available online: https://www.researchgate.net/publication/278704818_Self-Organizing_Artificial_Neural_Networks_into_Hydrographic_Big_Data_Reduction_Process (accessed on 12 September 2025).
64. Wlodarczyk-Sielicka, M.; Blaszczak-Bak, W. Processing of Bathymetric Data: The Fusion of New Reduction Methods for Spatial Big Data. *Sensors* **2020**, *20*, 6207, doi:10.3390/s20216207.
65. Li, J.; Heap, A.D.; Potter, A.; Huang, Z.; Daniell, J.J. Can We Improve the Spatial Predictions of Seabed Sediments? A Case Study of Spatial Interpolation of Mud Content across the Southwest Australian Margin. *Continental Shelf Research* **2011**, *31*, 1365–1376, doi:10.1016/j.csr.2011.05.015.
66. Yun, S.-J.; Kim, H.-G.; Park, J.-W.; Lee, H.-J.; Kim, J.-C.; Hwang, J.-H.; Choi, Y.-H.; Lee, S.-J.; Ryu, J.-K.; Suh, J.-H.; et al. Development of a Towed Underwater Platform That Can Operate in a Marine Environment and Explore the Sea Bottom. *Journal of Marine Science and Engineering* **2022**, *10*, 66, doi:10.3390/jmse10010066.
67. Amante, C.J.; Eakins, B.W. Accuracy of Interpolated Bathymetry in Digital Elevation Models. *Journal of Coastal Research* **2016**, 123–133, doi:10.2112/SI76-011.
68. Alcaras, E.; Amoroso, P.P.; Parente, C. The Influence of Interpolated Point Location and Density on 3D Bathymetric Models Generated by Kriging Methods: An Application on the Giglio Island Seabed (Italy). *Geosciences* **2022**, *12*, 62, doi:10.3390/geosciences12020062.
69. Simons, D.G.; Snellen, M. A Bayesian Approach to Seafloor Classification Using Multi-Beam Echo-Sounder Backscatter Data. *Applied Acoustics* **2009**, *70*, 1258–1268, doi:10.1016/j.apacoust.2008.07.013.
70. Menna, F.; Agrafiotis, P.; Georgopoulos, A. State of the Art and Applications in Archaeological Underwater 3D Recording and Mapping. *Journal of Cultural Heritage* **2018**, *33*, 231–248, doi:10.1016/j.culher.2018.02.017.
71. Hodúl, M.; Bird, S.; Knudby, A.; Chénier, R. Satellite Derived Photogrammetric Bathymetry. *ISPRS Journal of Photogrammetry and Remote Sensing* **2018**, *142*, 268–277, doi:10.1016/j.isprsjprs.2018.06.015.
72. Ernstsen, V.B.; Noormets, R.; Hebbeln, D.; Bartholomä, A.; Flemming, B.W. Precision of High-Resolution Multibeam Echo Sounding Coupled with High-Accuracy Positioning in a Shallow Water Coastal Environment. *Geo-Mar Lett* **2006**, *26*, 141–149, doi:10.1007/s00367-006-0025-3.
73. Brandt, D.; Lehmann, B. Acoustic 3D Reconstruction of Underwater Infrastructure – Possibilities, Problems & Potentials. **2025**, doi:10.5281/zenodo.17120720.
74. Nocerino, E.; Menna, F.; Fassi, F.; Remondino, F. UNDERWATER CALIBRATION OF DOME PORT PRESSURE HOUSINGS. *The International Archives of the Photogrammetry, Remote Sensing and Spatial Information Sciences* **2016**, *XL-3-W4*, 127–134, doi:10.5194/isprs-archives-XL-3-W4-127-2016.
75. Ghannami, M.A.; Daniel, S.; Sicot, G.; Quidu, I. A Likelihood-Based Triangulation Method for Uncertainties in Through-Water Depth Mapping. *Remote Sensing* **2024**, *16*, 4098, doi:10.3390/rs16214098.
76. Wen, K.; Li, Y.; Wang, H.; Jing, W.; Yang, J.; Zhang, C.; Wang, Z. Satellite-Based Water Depth Estimation: A Review. In; 2020; pp. 177–195 ISBN 978-981-15-6105-4.
77. Alevizos, E.; Alexakis, D.D. Evaluation of Radiometric Calibration of Drone-Based Imagery for Improving Shallow Bathymetry Retrieval. *Remote Sensing Letters* **2022**, *13*, 311–321, doi:10.1080/2150704X.2022.2030068.
78. He, J.; Zhang, S.; Cui, X.; Feng, W. Remote Sensing for Shallow Bathymetry: A Systematic Review. *Earth-Science Reviews* **2024**, *258*, 104957, doi:10.1016/j.earscirev.2024.104957.

 doi:10.20944/preprints202606.0385.v1

79. Caldareri, F.; Sulli, A.; Parrino, N.; Dardanelli, G.; Todaro, S.; Maltese, A. On the Shoreline Monitoring via Earth Observation: An Isoradiometric Method. *Remote Sensing of Environment* **2024**, *311*, 114286, doi:10.1016/j.rse.2024.114286.
80. Legleiter, C.J.; Roberts, D.A.; Lawrence, R.L. Spectrally Based Remote Sensing of River Bathymetry. *Earth Surface Processes and Landforms* **2009**, *34*, 1039–1059, doi:10.1002/esp.1787.
81. Chandrasekhar, S. Radiative Transfer. By S. Chandrasekhar. *Quarterly Journal of the Royal Meteorological Society* **1950**, *76*, 498–498, doi:10.1002/qj.49707633016.
82. Preisendorfer, R. Generalized Invariant Imbedding Relation. *Proceedings of the National Academy of Sciences* **1961**, *47*, 591–594, doi:10.1073/pnas.47.4.591.
83. Mobley, C.D. Trasferimento Radiativo Nell'oceano | Richiedi PDF Available online: https://www.researchgate.net/publication/286779947_Radiative_Transfer_in_the_Ocean (accessed on 7 October 2025).
84. Legleiter, C.J.; Roberts, D.A.; Lawrence, R.L. Spectrally Based Remote Sensing of River Bathymetry. *Earth Surface Processes and Landforms* **2009**, *34*, 1039–1059, doi:10.1002/esp.1787.
85. Abdallah, H.; Baghdadi, N.; Bailly, J.-S.; Pastol, Y.; Fabre, F. Wa-LiD: A New LiDAR Simulator for Waters. *IEEE Geoscience and Remote Sensing Letters* **2012**, *9*, 744–748, doi:10.1109/LGRS.2011.2180506.
86. Philpot, W. Bathymetric Mapping with Passive Multispectral Imagery. *Applied Optics* **1989**, *28*, 1569–1578, doi:10.1364/AO.28.001569.
87. Li, X.; Liu, C.; Wang, Z.; Xie, X.; Li, D.; Xu, L. Airborne LiDAR: State-of-the-Art of System Design, Technology and Application. *Meas. Sci. Technol.* **2020**, *32*, 032002, doi:10.1088/1361-6501/abc867.
88. Gallegos, C.L.; Moore, K.A. Factors contributing to water-column light attenuation. **2000**.
89. Jamet, C.; Loisel, H.; Dessailly, D. Retrieval of the Spectral Diffuse Attenuation Coefficient Kd(λ) in Open and Coastal Ocean Waters Using a Neural Network Inversion. *Journal of Geophysical Research: Oceans* **2012**, *117*, doi:10.1029/2012JC008076.
90. Lee, Z.-P.; Darecki, M.; Carder, K.L.; Davis, C.O.; Stramski, D.; Rhea, W.J. Diffuse Attenuation Coefficient of Downwelling Irradiance: An Evaluation of Remote Sensing Methods. *Journal of Geophysical Research: Oceans* **2005**, *110*, doi:10.1029/2004JC002573.
91. Stumpf, R.P.; Holderied, K.; Sinclair, M. Determination of Water Depth with High-Resolution Satellite Imagery over Variable Bottom Types. *Limnology and Oceanography* **2003**, *48*, 547–556, doi:10.4319/lo.2003.48.1_part_2.0547.
92. Lyzenga, D. Shallow-Water Bathymetry Using Combined Lidar and Passive Multispectral Scanner Data. *International Journal of Remote Sensing* **1985**, *6*, 115–125, doi:10.1080/01431168508948428.
93. Lyzenga, D.; Malinas, N.; Tanis, F.J. Multispectral Bathymetry Using a Simple Physically Based Algorithm. *Geoscience and Remote Sensing, IEEE Transactions on* **2006**, *44*, 2251–2259, doi:10.1109/TGRS.2006.872909.
94. Nocera, G.A.; Presti, V.L.; Sulli, A.; Maltese, A. Improving the Accuracy of Optical Satellite-Derived Bathymetry Through High Spatial, Spectral, and Temporal Resolutions. *Remote Sensing* **2026**, *18*, doi:10.3390/rs18020270.
95. Danesh-Yazdi, M.; Bayati, M.; Tajrishy, M.; Chehrenegar, B. Revisiting Bathymetry Dynamics in Lake Urmia Using Extensive Field Data and High-Resolution Satellite Imagery. *Journal of Hydrology* **2021**, *603*, 126987, doi:10.1016/j.jhydrol.2021.126987.
96. Gholamalifard, M.; Sari, A.; Abkar, A.; Naimi, B. Bathymetric Modeling from Satellite Imagery via Single Band Algorithm (SBA) and Principal Components Analysis (PCA) in Southern Caspian Sea. *International Journal of Environmental Research* **2013**, *7*, 877–886.
97. El-Mewafi, M.; Salah, M.; Fawzi, B. Assessment of Optical Satellite Images for Bathymetry Estimation in Shallow Areas Using Artificial Neural Network Model. *American Journal of Geographic Information System* **2018**, *7*, 99–106.
98. Róg, M.; Rzonca, A. The Impact of Photo Overlap, the Number of Control Points and the Method of Camera Calibration on the Accuracy of 3D Model Reconstruction. *Geomatics and Environmental Engineering* **2021**, *15*, 67, doi:10.7494/geom.2021.15.2.67.
99. Murase, T. A Photogrammetric Correction Procedure for Light Refraction Effects at a Two-Medium Boundary. *PHOTOGRAMMETRIC ENGINEERING* **2008**.

 doi:10.20944/preprints202606.0385.v1

100. Kraus, K.; Harley, I.; Kraus, K. *Photogrammetry: Geometry from Images and Laser Scans*; De Gruyter Textbook; 2. ed.; de Gruyter: Berlin, 2007; ISBN 978-3-11-019007-6.
101. Ismail, M. Snell's Law from Heisenberg's Uncertainty Principle. **2020**.
102. Doneus, M.; Doneus, N.; Briese, C.; Pregesbauer, M.; Mandlburger, G.; Verhoeven, G. Airborne Laser Bathymetry – Detecting and Recording Submerged Archaeological Sites from the Air. *Journal of Archaeological Science* **2013**, *40*, 2136–2151, doi:10.1016/j.jas.2012.12.021.
103. Cao, B.; Deng, R.; Zhu, S. Universal Algorithm for Water Depth Refraction Correction in Through-Water Stereo Remote Sensing. *International Journal of Applied Earth Observation and Geoinformation* **2020**, *91*, 102108, doi:10.1016/j.jag.2020.102108.
104. Maas, H.-G. On the Accuracy Potential in Underwater/Multimedia Photogrammetry. *Sensors* **2015**, *15*, 18140–18152, doi:10.3390/s150818140.
105. Menna, F.; Nocerino, E.; Remondino, F. FLAT VERSUS HEMISPHERICAL DOME PORTS IN UNDERWATER PHOTOGRAMMETRY. *The International Archives of the Photogrammetry, Remote Sensing and Spatial Information Sciences* **2017**, *XLII-2-W3*, 481–487, doi:10.5194/isprs-archives-XLII-2-W3-481-2017.
106. Woodget, A.S.; Carbonneau, P.E.; Visser, F.; Maddock, I.P. Quantifying Submerged Fluvial Topography Using Hyperspatial Resolution UAS Imagery and Structure from Motion Photogrammetry. *Earth Surface Processes and Landforms* **2015**, *40*, 47–64, doi:10.1002/esp.3613.
107. Dietrich, J. Bathymetric Structure from Motion: Extracting Shallow Stream Bathymetry from Multi-View Stereo Photogrammetry. *Earth Surface Processes and Landforms* **2017**, *42*, 355–364, doi:10.1002/esp.4060.
108. Partama, I.G. A Simple and Empirical Refraction Correction Method for UAV-Based Shallow-Water Photogrammetry. *International Journal of Environmental, Chemical, Ecological, Geological and Geophysical Engineering* **2017**, *11*, 254–261.
109. Mulsow, C. A FLEXIBLE MULTI-MEDIA BUNDLE APPROACH. **2010**.
110. Schönberger, J.; Frahm, J.-M. *Structure-from-Motion Revisited*; 2016;
111. Hirschmuller, H. Stereo Processing by Semiglobal Matching and Mutual Information | IEEE Journals & Magazine | IEEE Xplore Available online: https://ieeexplore.ieee.org/document/4359315 (accessed on 22 October 2025).
112. Remondino, F.; Spera, M.G.; Nocerino, E.; Menna, F.; Nex, F. State of the Art in High Density Image Matching. *The Photogrammetric Record* **2014**, *29*, 144–166, doi:10.1111/phor.12063.
113. Agrafiotis, P.; Karantzalos, K.; Georgopoulos, A.; Skarlatos, D. Correcting Image Refraction: Towards Accurate Aerial Image-Based Bathymetry Mapping in Shallow Waters. *Remote Sensing* **2020**, *12*, 322, doi:10.3390/rs12020322.
114. Castillón, M.; Palomer, A.; Forest, J.; Ridao, P. State of the Art of Underwater Active Optical 3D Scanners. *Sensors* **2019**, *19*, 5161, doi:10.3390/s19235161.
115. Mandlburger, G. A REVIEW OF ACTIVE AND PASSIVE OPTICAL METHODS IN HYDROGRAPHY. *IHR* 2022.
116. Xiao, X.; Jiang, Z.; Xu, W.; Guo, Y.; Liu, Y.; Guo, Z. The Influence of Refractive Index Changes in Water on Airborne LiDAR Bathymetric Errors. *Journal of Marine Science and Engineering* **2024**, *12*, 435, doi:10.3390/jmse12030435.
117. Wu, L.; Chen, Y.; Le, Y.; Zhang, D.; Zhang, X.; Wang, L. GeologyObserver-1: A Dual-Frequency Photon-Counting LiDAR UAV Detection System for 3-D Land and Water Mapping. *IEEE Journal on Miniaturization for Air and Space Systems* **2025**, *6*, 209–214, doi:10.1109/JMASS.2025.3541783.
118. Degnan, J.J. Scanning, Multibeam, Single Photon Lidars for Rapid, Large Scale, High Resolution, Topographic and Bathymetric Mapping. *Remote Sensing* **2016**, *8*, 958, doi:10.3390/rs8110958.
119. Swatantran, A.; Tang, H.; Barrett, T.; DeCola, P.; Dubayah, R. Rapid, High-Resolution Forest Structure and Terrain Mapping over Large Areas Using Single Photon Lidar. *Sci Rep* **2016**, *6*, 28277, doi:10.1038/srep28277.
120. Chen, Y.; Le, Y.; Wu, L.; Li, S.; Wang, L. An Assessment of Waveform Processing for a Single-Beam Bathymetric LiDAR System (SBLS-1). *Sensors* **2022**, *22*, 7681, doi:10.3390/s22197681.
121. Wang, C.; Li, Q.; Liu, Y.; Wu, G.; Liu, P.; Ding, X. A Comparison of Waveform Processing Algorithms for Single-Wavelength LiDAR Bathymetry. *ISPRS Journal of Photogrammetry and Remote Sensing* **2015**, *101*, 22–35, doi:10.1016/j.isprsjprs.2014.11.005.

 doi:10.20944/preprints202606.0385.v1

122. Pfennigbauer, M.; Wolf, C.; Weinkopf, J.; Ullrich, A. Online Waveform Processing for Demanding Target Situations. **2014**.
123. Wagner, W.; Ullrich, A.; Melzer, T.; Briese, C.; Kraus, K. *From Singleâ˜“pulse to Full-Waveform Airborne Laser Scanners: Potential and Practical Challenges*; 2004; Vol. 35, p. 206;.
124. Wagner, W.; Roncat, A.; Melzer, T.; Ullrich, A. Waveform Analysis Techniques in Airborne Laser Scanning. **2007**.
125. Jutzi, B.; Stilla, U. Range Determination with Waveform Recording Laser Systems Using a Wiener Filter. *ISPRS Journal of Photogrammetry and Remote Sensing* **2006**, *61*, 95–107, doi:10.1016/j.isprsjprs.2006.09.001.
126. Wu, J.; van Aardt, J.A.N.; Asner, G.P. A Comparison of Signal Deconvolution Algorithms Based on Small-Footprint LiDAR Waveform Simulation. *IEEE Transactions on Geoscience and Remote Sensing* **2011**, *49*, 2402–2414, doi:10.1109/TGRS.2010.2103080.
127. Chauve, A.; Mallet, C.; Bretar, F.; Durrieu, S.; Pierrot-Deseilligny, M.; Puech, W. Processing Full-Waveform Lidar Data: Modelling Raw Signals.; September 12 2007; Vol. 36 (Part 3/W52), p. 102.
128. Abady, L.; Bailly, J.-S.; Baghdadi, N.; Pastol, Y.; Abdallah, H. Assessment of Quadrilateral Fitting of the Water Column Contribution in Lidar Waveforms on Bathymetry Estimates. *IEEE Geoscience and Remote Sensing Letters* **2014**, *11*, 813–817, doi:10.1109/LGRS.2013.2279271.
129. Cao, B.; Wang, J.; Hu, Y.; Lv, Y.; Yang, X.; Gong, H.; Li, G.; Lu, X. ICESAT-2 Shallow Bathymetric Mapping Based on a Size and Direction Adaptive Filtering Algorithm. *IEEE Journal of Selected Topics in Applied Earth Observations and Remote Sensing* **2023**, *16*, 6279–6295, doi:10.1109/JSTARS.2023.3290672.
130. Shangguan, M.; Weng, Z.; Lin, Z.; Lee, Z.; Shangguan, M.; Yang, Z.; Sun, J.; Wu, T.; Zhang, Y.; Wen, C. Day and Night Continuous High-Resolution Shallow-Water Depth Detection with Single-Photon Underwater Lidar. *Opt. Express, OE* **2023**, *31*, 43950–43962, doi:10.1364/OE.505865.
131. Jung, J.; Parrish, C.E.; Magruder, L.A.; Herrmann, J.; Yoo, S.; Perry, J.S. ICESat-2 Bathymetry Algorithms: A Review of the Current State-of-the-Art and Future Outlook. *ISPRS Journal of Photogrammetry and Remote Sensing* **2025**, *223*, 413–439, doi:10.1016/j.isprsjprs.2025.03.016.
132. Cao, B.; Yong, F.; Gao, L.; Hu, H.; Jiang, Z.; Sun, B.; Lou, L. An Active-Passive Fusion Strategy and Accuracy Evaluation for Shallow Water Bathymetry Based on ICESat-2 ATLAS Laser Point Cloud and Satellite Remote Sensing Imagery. *International Journal of Remote Sensing* **2021**, *42*, 2783–2806, doi:10.1080/01431161.2020.1862441.
133. Ma, Y.; Xu, N.; Liu, Z.; Yang, B.; Yang, F.; Wang, X.H.; Li, S. Satellite-Derived Bathymetry Using the ICESat-2 Lidar and Sentinel-2 Imagery Datasets. *Remote Sensing of Environment* **2020**, *250*, 112047, doi:10.1016/j.rse.2020.112047.
134. Wei, G.; Shalei, S.; Bo, Z.; Shuo, S.; Faquan, L.; Xuewu, C. Multi-Wavelength Canopy LiDAR for Remote Sensing of Vegetation: Design and System Performance. *ISPRS Journal of Photogrammetry and Remote Sensing* **2012**, *69*, 1–9, doi:10.1016/j.isprsjprs.2012.02.001.
135. Del Savio, A.A.; Luna Torres, A.; Vergara Olivera, M.A.; Llimpe Rojas, S.R.; Urday Ibarra, G.T.; Neckel, A. Using UAVs and Photogrammetry in Bathymetric Surveys in Shallow Waters. *Applied Sciences* **2023**, *13*, 3420, doi:10.3390/app13063420.
136. Schwarz, R.; Mandlburger, G.; Pfennigbauer, M.; Pfeifer, N. Design and Evaluation of a Full-Wave Surface and Bottom-Detection Algorithm for LiDAR Bathymetry of Very Shallow Waters. *ISPRS Journal of Photogrammetry and Remote Sensing* **2019**, *150*, 1–10, doi:10.1016/j.isprsjprs.2019.02.002.
137. Cao, B.; Fang, Y.; Jiang, Z.; Gao, L.; Hu, H. Shallow Water Bathymetry from WorldView-2 Stereo Imagery Using Two-Media Photogrammetry. *European Journal of Remote Sensing* **2019**, *52*, 506–521, doi:10.1080/22797254.2019.1658542.
138. Pereira, P.; Baptista, P.; Cunha, T.; Silva, P.A.; Romão, S.; Lafon, V. Estimation of the Nearshore Bathymetry from High Temporal Resolution Sentinel-1A C-Band SAR Data - A Case Study. *Remote Sensing of Environment* **2019**, *223*, 166–178, doi:10.1016/j.rse.2019.01.003.
139. Westfeld, P.; Maas, H.-G.; Richter, K.; Weiß, R. Analysis and Correction of Ocean Wave Pattern Induced Systematic Coordinate Errors in Airborne LiDAR Bathymetry. *ISPRS Journal of Photogrammetry and Remote Sensing* **2017**, *128*, 314–325, doi:10.1016/j.isprsjprs.2017.04.008.

 doi:10.20944/preprints202606.0385.v1

140. Duplančić Leder, T.; Baučić, M.; Leder, N.; Gilić, F. Optical Satellite-Derived Bathymetry: An Overview and WoS and Scopus Bibliometric Analysis. *Remote Sensing* **2023**, *15*, 1294, doi:10.3390/rs15051294.
141. Specht, O. Spatial Analysis of Bathymetric Data from UAV Photogrammetry and ALS LiDAR: Shallow-Water Depth Estimation and Shoreline Extraction. *Remote Sensing* **2025**, *17*, 3115, doi:10.3390/rs17173115.
142. Petras, V.; Petrasova, A.; McCarter, J.B.; Mitasova, H.; Meentemeyer, R.K. Point Density Variations in Airborne Lidar Point Clouds. *Sensors* **2023**, *23*, 1593, doi:10.3390/s23031593.
143. Chen, B.; Yang, Y.; Xu, D.; Huang, E. A Dual Band Algorithm for Shallow Water Depth Retrieval from High Spatial Resolution Imagery with No Ground Truth. *ISPRS Journal of Photogrammetry and Remote Sensing* **2019**, *151*, 1–13, doi:10.1016/j.isprsjprs.2019.02.012.
144. Wu, Y.; Shi, H.; Jia, D.; Andersen, O.B.; He, X.; Luo, Z.; Li, Y.; Chen, S.; Si, X.; Diao, S.; et al. HHU24SWDSCS: A Shallow-Water Depth Model over Island Areas in the South China Sea Retrieved from Satellite-Derived Bathymetry. *Earth System Science Data* **2025**, *17*, 2463–2488, doi:10.5194/essd-17-2463-2025.
145. Raffa, F.; Alberico, I.; Serafino, F. X-Band Radar System to Detect Bathymetric Changes at River Mouths during Storm Surges: A Case Study of the Arno River. *Sensors* **2022**, *22*, 9415, doi:10.3390/s22239415.
146. Pereira, P.; Baptista, P.; Cunha, T.; Silva, P.A.; Romão, S.; Lafon, V. Estimation of the Nearshore Bathymetry from High Temporal Resolution Sentinel-1A C-Band SAR Data - A Case Study. *Remote Sensing of Environment* **2019**, *223*, 166–178, doi:10.1016/j.rse.2019.01.003.
147. Bergsma, E.W.J.; Almar, R.; Maisongrande, P. Radon-Augmented Sentinel-2 Satellite Imagery to Derive Wave-Patterns and Regional Bathymetry. *Remote Sensing* **2019**, *11*, 1918, doi:10.3390/rs11161918.
148. Simarro, G. Influence of Bed Variations on Linear Wave Propagation beyond the Mild Slope Condition. *Journal of Marine Science and Engineering* **2024**, *12*, 1652, doi:10.3390/jmse12091652.
149. Magdalena, I.; Pudjaprasetya, S.R. Numerical Modeling of 2D Wave Refraction and Shoaling Available online: https://www.researchgate.net/publication/262951997_Numerical_Modeling_of_2D_Wave_Refraction_and_Shoaling (accessed on 10 December 2025).
150. Farhad, S. Shoaling, Refraction and Diffraction in Waves Available online: https://www.researchgate.net/publication/390824297_Shoaling_Refraction_and_Diffraction_in_Waves (accessed on 10 December 2025).
151. Holthuijsen, L. Waves in Oceanic and Coastal Waters Available online: https://www.researchgate.net/publication/253127661_Waves_in_Oceanic_and_Coastal_Waters (accessed on 15 December 2025).
152. Brusch, S.; Held, P.; Lehner, S.; Rosenthal, W.; Pleskachevsky, A. Underwater Bottom Topography in Coastal Areas from TerraSAR-X Data. *International Journal of Remote Sensing* **2011**, *32*, 4527–4543, doi:10.1080/01431161.2010.489063.
153. Almar, R.; Bergsma, E.W.J.; Maisongrande, P.; de Almeida, L.P.M. Wave-Derived Coastal Bathymetry from Satellite Video Imagery: A Showcase with Pleiades Persistent Mode. *Remote Sensing of Environment* **2019**, *231*, 111263, doi:10.1016/j.rse.2019.111263.
154. Kudryavtsev, V.; Yurovskaya, M.; Chapron, B.; Collard, F.; Donlon, C. Sun Glitter Imagery of Ocean Surface Waves. Part 1: Directional Spectrum Retrieval and Validation. *Journal of Geophysical Research: Oceans* **2017**, *122*, 1369–1383, doi:10.1002/2016JC012425.
155. Klotz, A.N.; Almar, R.; Quenet, Y.; Bergsma, E.W.J.; Youssefi, D.; Artigues, S.; Rascle, N.; Sy, B.A.; Ndour, A. Nearshore Satellite-Derived Bathymetry from a Single-Pass Satellite Video: Improvements from Adaptive Correlation Window Size and Modulation Transfer Function. *Remote Sensing of Environment* **2024**, *315*, 114411, doi:10.1016/j.rse.2024.114411.
156. Kudryavtsev, V.; Yurovskaya, M.; Chapron, B.; Collard, F.; Donlon, C. Sun Glitter Imagery of Ocean Surface Waves. Part 1: Directional Spectrum Retrieval and Validation. *Journal of Geophysical Research: Oceans* **2017**, *122*, 1369–1383, doi:10.1002/2016JC012425.
157. Xie, Y.; Li, Y.; Yang, J.; Xu, J.; Deng, Y. *Geoinformatics in Sustainable Ecosystem and Society: 7th International Conference, GSES 2019, and First International Conference, GeoAI 2019, Guangzhou, China, November 21–25, 2019, Revised Selected Papers*; Communications in Computer and Information Science, 1228; 1st ed. 2020.; Springer Singapore: Singapore, 2020; ISBN 978-981-15-6106-1.

 doi:10.20944/preprints202606.0385.v1

158. de Michele, M.; Leprince, S.; Thiébot, J.; Raucoules, D.; Binet, R. Direct Measurement of Ocean Waves Velocity Field from a Single SPOT-5 Dataset. *Remote Sensing of Environment* **2012**, *119*, 266–271, doi:10.1016/j.rse.2011.12.014.
159. Dronkers, J. Batimetria Dalla Propagazione Delle Onde Tramite Telerilevamento - Coastal Wiki Available online: https://www.coastalwiki.org/wiki/Bathymetry_from_remote_sensing_wave_propagation (accessed on 15 December 2025).
160. Vesecky, J.F.; Stewart, R.H. The Observation of Ocean Surface Phenomena Using Imagery from the SEASAT Synthetic Aperture Radar: An Assessment. *Journal of Geophysical Research: Oceans* **1982**, *87*, 3397–3430, doi:10.1029/JC087iC05p03397.
161. Almar, R.; Bergsma, E.W.J.; Thoumyre, G.; Baba, M.W.; Cesbron, G.; Daly, C.; Garlan, T.; Lifermann, A.; Almar, R.; Bergsma, E.W.J.; et al. Global Satellite-Based Coastal Bathymetry from Waves. *Remote Sensing* **2021**, *13*, doi:10.3390/rs13224628.
162. Martin, S. *An Introduction to Ocean Remote Sensing*; Cambridge University Press, 2014; ISBN 978-1-139-91615-8.
163. Sarsito, D.; Syahrullah, M.; Wijaya, D.; Pradipta, D.; Andreas, H. Studying Dynamic Ocean Topography in Indonesia Sea Based on Satellite Altimetry. *IOP Conference Series: Earth and Environmental Science* **2021**, *925*, 012062, doi:10.1088/1755-1315/925/1/012062.
164. Heiskanen, A.; Helmut, M. Physical Geodesy Available online: https://it.scribd.com/document/496304127/Weikko-A-Heiskanen-Helmut-Moritz-Physical-Geodesy-W-H-Freeman-Co-Ltd-1967 (accessed on 3 December 2025).
165. Kim, J.W.; von Frese, R.R.B.; Lee, B.Y.; Roman, D.R.; Doh, S.-J. Altimetry-Derived Gravity Predictions of Bathymetry by the Gravity-Geologic Method. *Pure Appl. Geophys.* **2011**, *168*, 815–826, doi:10.1007/s00024-010-0170-5.
166. Sandwell, D.T.; Smith, W.H.F.; Gille, S.; Kappel, E.; Jayne, S.; Soofi, K.; Coakley, B.; Géli, L. Bathymetry from Space: Rationale and Requirements for a New, High-Resolution Altimetric Mission. *Comptes Rendus Geoscience* **2006**, *338*, 1049–1062, doi:10.1016/j.crte.2006.05.014.
167. Vrdoljak, L.; Bašić, T.; Vrdoljak, L.; Bašić, T. Bathymetry Estimation from Satellite Altimeter-Derived Gravity Data. In *Satellite Altimetry - Theory, Applications and Recent Advances*; IntechOpen, 2022 ISBN 978-1-80355-880-6.
168. Chen, X.; Yang, M.; Sun, M.; Li, W.; An, D.; Feng, P.; Feng, W.; Zhong, M. Enhancing Bathymetry Estimation from Altimeter-Derived Gravity in Shallow to Intermediate Seas by Integrating Coastline and SDB Constraints. *Advances in Space Research* **2025**, *76*, 4959–4976, doi:10.1016/j.asr.2025.07.094.
169. Liu, P.; Jin, S.; Wu, Z. Assessment of the Seafloor Topography Accuracy in the Emperor Seamount Chain by Ship-Based Water Depth Data and Satellite-Based Gravity Data. *Sensors* **2022**, *22*, 3189, doi:10.3390/s22093189.
170. Smith, W.H.; Sandwell, D.T. Global Sea Floor Topography from Satellite Altimetry and Ship Depth Soundings. *Science* **1997**, *277*, 1956–1962, doi:10.1126/science.277.5334.1956.
171. Parker, R.L. The Rapid Calculation of Potential Anomalies. *Geophysical Journal International* **1973**, *31*, 447–455, doi:10.1111/j.1365-246X.1973.tb06513.x.
172. Vermeer, M. Physical Geodesy. **2020**.
173. Kim, K.B.; Kim, J.; Yun, H.S. Improved Bathymetry Estimation Using Satellite Altimetry-Derived Gravity Anomalies and Machine Learning in the East Sea. *Journal of Marine Science and Engineering* **2024**, *12*, 1520, doi:10.3390/jmse12091520.
174. Dettmering, D.; Ellenbeck, L.; Scherer, D.; Schwatke, C.; Niemann, C.; Dettmering, D.; Ellenbeck, L.; Scherer, D.; Schwatke, C.; Niemann, C. Potential and Limitations of Satellite Altimetry Constellations for Monitoring Surface Water Storage Changes—A Case Study in the Mississippi Basin. *Remote Sensing* **2020**, *12*, doi:10.3390/rs12203320.
175. Watts, A.B.; Sandwell, D.T.; Smith, W.H.F.; Wessel, P. Global Gravity, Bathymetry, and the Distribution of Submarine Volcanism through Space and Time. *Journal of Geophysical Research: Solid Earth* **2006**, *111*, doi:10.1029/2005JB004083.

 doi:10.20944/preprints202606.0385.v1

176. Smith, W.H.F.; Sandwell, D.T.; Raney, R.K. (PDF) Bathymetry from satellite altimetry: Present and future. In Proceedings of the ResearchGate; 2005.
177. Sardemann, H.; Mulsow, C.; Maas, H.-G. Accuracy Analysis of an Oblique Underwater Laser Lightsheet Triangulation System. *PFG* **2022**, *90*, 3–18, doi:10.1007/s41064-022-00196-x.
178. Hobson, P.R.; Watson, J. Accurate Three-Dimensional Metrology of Underwater Objects Using Replayed Real Images from in-Line and off-Axis Holograms. *Meas. Sci. Technol.* **1999**, *10*, 1153, doi:10.1088/0957-0233/10/12/306.
179. Xie, S.-P.; Hafner, J.; Tanimoto, Y.; Liu, W.T.; Tokinaga, H.; Xu, H. Bathymetric Effect on the Winter Sea Surface Temperature and Climate of the Yellow and East China Seas. *Geophysical Research Letters* **2002**, *29*, 81-1-81–84, doi:10.1029/2002GL015884.
180. Park, K.-A.; Chung, J.Y.; Kim, K.; Cornillon, P.C. Wind and Bathymetric Forcing of the Annual Sea Surface Temperature Signal in the East (Japan) Sea. *Geophysical Research Letters* **2005**, *32*, doi:10.1029/2004GL022197.
181. Balsamo, G.; Dutra, E.; Stepanenko, V.M.; Viterbo, P.; Miranda, P.M.; Mironov, D. Technical Memorandum. *Deriving an effective lake depth from satellite lake surface temperature: A feasibility study with MODIS data* **2010**.
182. Kessler, J.; Espey, E.; VanDeWeghe, A.; Gronewold, A.D.; Sorensen, T.; Khazaei, B.; James, E.; Smirnova, T.G.; Casali, M.; Yates, D.; et al. Depth Matters: Lake Bathymetry Selection in Numerical Weather Prediction Systems. *Journal of Geophysical Research: Atmospheres* **2025**, *130*, e2024JD041794, doi:10.1029/2024JD041794.
183. Liu, Y.; Gao, X.; Wang, G.; Zhang, T.; Wang, J. A METHOD OF WATER DEPTH INVERSION IN COASTAL AREA CONSIDERING TEMPERATURE INFORMATION. *ISPRS Annals of the Photogrammetry, Remote Sensing and Spatial Information Sciences* **2021**, *V-3–2021*, 23–28, doi:10.5194/isprs-annals-V-3-2021-23-2021.
184. Karimi, N.; Torabi, O. Remote Sensing-Based Bathymetry Mapping in Shallow Lakes: Comparative Analysis of Sentinel-2 and Landsat-8 Imagery Integrated with Machine Learning Techniques. *Advances in Space Research* **2025**, doi:10.1016/j.asr.2025.10.028.
185. Sambuelli, L.; Bava, S. Case Study: A GPR Survey on a Morainic Lake in Northern Italy for Bathymetry, Water Volume and Sediment Characterization. *Journal of Applied Geophysics* **2012**, *81*, 48–56, doi:10.1016/j.jappgeo.2011.09.016.
186. Bandini, F.; Kooij, L.; Mortensen, B.K.; Caspersen, M.B.; Thomsen, L.G.; Olesen, D.; Bauer-Gottwein, P. Mapping Inland Water Bathymetry with Ground Penetrating Radar (GPR) on Board Unmanned Aerial Systems (UASs). *Journal of Hydrology* **2023**, *616*, 128789, doi:10.1016/j.jhydrol.2022.128789.
187. Jawak, S.D.; Vadlamani, S.S.; Luis, A.J. A Synoptic Review on Deriving Bathymetry Information Using Remote Sensing Technologies: Models, Methods and Comparisons. *Advances in Remote Sensing* **2015**, *4*, 147–162, doi:10.4236/ars.2015.42013.
188. Weatherall, P.; Marks, K.M.; Jakobsson, M.; Schmitt, T.; Tani, S.; Arndt, J.E.; Rovere, M.; Chayes, D.; Ferrini, V.; Wigley, R. A New Digital Bathymetric Model of the World's Oceans. *Earth and Space Science* **2015**, *2*, 331–345, doi:10.1002/2015EA000107.
189. Gaida, T.C.; Mohammadloo, T.H.; Snellen, M.; Simons, D.G. Mapping the Seabed and Shallow Subsurface with Multi-Frequency Multibeam Echosounders. *Remote Sensing* **2019**, *12*, doi:10.3390/rs12010052.
190. Gao, J. Bathymetric Mapping by Means of Remote Sensing: Methods, Accuracy and Limitations. *Progress in Physical Geography: Earth and Environment* **2009**, *33*, 103–116, doi:10.1177/0309133309105657.
191. Direttiva Habitat - Ambiente - Commissione Europea Available online: https://environment.ec.europa.eu/topics/nature-and-biodiversity/habitats-directive_en (accessed on 4 March 2026).
192. Wu, Y.; Shi, H.; Jia, D.; Andersen, O.B.; He, X.; Luo, Z.; Li, Y.; Chen, S.; Si, X.; Diao, S.; et al. HHU24SWDSCS: A Shallow-Water Depth Model over Island Areas in the South China Sea Retrieved from Satellite-Derived Bathymetry. *Earth System Science Data* **2025**, *17*, 2463–2488, doi:10.5194/essd-17-2463-2025.
193. Thomson, D.; Elson, S. New Generation Acoustic Positioning Systems. In Proceedings of the Oceans Conf Rec IEEE; 2002; Vol. 3, pp. 1312–1318.
194. Lo, E.; Lozano Bravo, H.; Hui, N.; Nocerino, E.; Menna, F.; Rissolo, D.; Kuester, F. Evaluation of the Accuracy of Photogrammetric Reconstruction of Bathymetry Using Differential GNSS Synchronized with an Underwater Camera. *Int. Arch. Photogramm. Remote Sens. Spatial Inf. Sci.* **2024**, *XLVIII-2–2024*, 211–218, doi:10.5194/isprs-archives-XLVIII-2-2024-211-2024.

 doi:10.20944/preprints202606.0385.v1

195. Das, S.; Chatterjee, B.; Roy Choudhury, M.; Dutta, S.; Mondal, B.P.; Awasthi, A. Synthetic Aperture Radar for a Changing Planet: A 25-Year Global Synthesis in Hazard Assessment, Urban Development, and Ecological Applications. *Ecological Informatics* **2025**, *92*, 103477, doi:10.1016/j.ecoinf.2025.103477.
196. Gao, X.; Shen, S.; Hu, Z.; Wang, Z. Ground and Aerial Meta-Data Integration for Localization and Reconstruction: A Review. *Pattern Recognition Letters* **2019**, *127*, 202–214, doi:10.1016/j.patrec.2018.07.036.